POLITECNICO DI TORINO
Repository ISTITUZIONALE

Long-time rigidity to flux-induced symmetry breaking in quantum quench dynamics

Original
Long-time rigidity to flux-induced symmetry breaking in quantum quench dynamics / Rossi, Lorenzo; Barbiero, Luca; Budich, Jan Carl; Dolcini, Fabrizio. - In: PHYSICAL REVIEW. B. - ISSN 2469-9950. - STAMPA. - 108:15(2023). [10.1103/PhysRevB.108.155420]

Availability:
This version is available at: 11583/2983296 since: 2023-11-28T10:15:18Z

Publisher:
American Physical Society

Published
DOI:10.1103/PhysRevB.108.155420

Terms of use:

This article is made available under terms and conditions as specified in the corresponding bibliographic description in the repository

Publisher copyright
APS postprint/Author's Accepted Manuscript e postprint versione editoriale/Version of Record

This article appeared in PHYSICAL REVIEW. B, 2023, 108, 15, and may be found at ttp://dx.doi.org/10.1103/PhysRevB.108.155420. Copyright 2023 American Physical Society

(Article begins on next page)

07 May 2026

Long-time rigidity to flux-induced symmetry breaking in quantum quench dynamics

Lorenzo Rossi [1], Luca Barbiero [1], Jan Carl Budich [2] and Fabrizio Dolcini [1,*]

[1] *Dipartimento di Scienza Applicata e Tecnologia, Politecnico di Torino, 10129 Torino, Italy*

[2] *Institute of Theoretical Physics, Technische Universität Dresden and Würzburg-Dresden Cluster of Excellence ct.qmat, 01062 Dresden, Germany*

(Received 7 July 2023; accepted 5 October 2023; published 18 October 2023)

We investigate how the breaking of charge conjugation symmetry $\mathcal{C}$ impacts on the dynamics of a half-filled fermionic lattice system after global quenches. We show that, when the initial state is insulating and the $\mathcal{C}$ symmetry is broken nonlocally by a constant magnetic flux, local observables, and correlations behave as if the symmetry were unbroken for a time interval proportional to the system size L. In particular, the local particle density of a quenched dimerized insulator remains pinned to $1/2$ in each lattice site for an extensively long time, while it starts to significantly fluctuate only afterwards. Due to its qualitative resemblance to the sudden arrival of rapidly rising ocean waves, we dub this phenomenon the "tsunami effect." Notably, it occurs even though the chiral symmetry is dynamically broken right after the quench. Furthermore, we identify a way to quantify the amount of symmetry breaking in the quantum state, showing that in insulators perturbed by a flux, it is exponentially suppressed as a function of the system size, while it is only algebraically suppressed in metals and in insulators with locally broken $\mathcal{C}$ symmetry. The robustness of the tsunami effect to weak disorder and interactions is demonstrated, and possible experimental realizations are proposed.

DOI: 10.1103/PhysRevB.108.155420

I. INTRODUCTION

One of the most surprising aspects of quantum mechanics is the nonlocal effect induced by a magnetic flux. Indeed, in striking contrast to classical particles, a charged quantum particle can experience the presence of a flux even in regions where no magnetic field is present. The Aharonov-Bohm effect [1,2] is a paradigmatic manifestation of this phenomenon. Nevertheless, metals and insulators are known to exhibit a quite different response to a magnetic flux, encoded within the linear response theory in the Drude weight D [3–6]. Such a quantity, which is obtained from equilibrium state correlation functions, describes the current generated by a flux-induced electric pulse. While D is finite for metals, it vanishes for an insulator, implying that the ground state energy of an insulator is insensitive to magnetic flux variations. It has also been proven that, as long as flux changes adiabatically, such insensitivity to a flux holds also beyond linear response theory, i.e., in higher order Drude weigths [7,8]. In this respect, insulators exhibit a more "classical behavior" than metals, in view of the localized character of their correlations [3].

In recent years, the experimental advances in cold atom setups [9–12] have motivated an intense theoretical activity to investigate the effects of a flux in far away from equilibrium settings, like in quantum quenches [13–16], where the adiabaticity condition does not hold. Most works have analyzed flux quenches in fermionic ring-shaped lattice systems, where a flux is suddenly switched on or off, mainly with the purpose of determining whether a persistent current can flow in these conditions, how it is possibly affected by interactions, and what is its nonlinear dependence on the flux [17–19].

It should be pointed out, however, that any flux quench protocol induces a *local* electric pulse, which is thus a classical effect *per se*. In order to probe genuine quantum mechanical nonlocal effects of the flux in the far from equilibrium dynamics, it is important to rather consider a constant magnetic flux, and to quench other parameters. In these conditions, a crucial question is still open: when an insulator is driven out of equilibrium, how long does it remain insensitive to the presence of a flux?

Interestingly, this type of problems can also be considered from a different perspective, namely the impact of symmetry breaking. In quantum systems, where the state is characterized by a density matrix operator $\boldsymbol{\rho}$ and its evolution is governed by the Hamiltonian H, one has to consider the effect of symmetries on both $\boldsymbol{\rho}$ and H, as they are not necessarily related. Indeed a Hamiltonian may fulfill a given symmetry, despite each of its degenerate ground states may not, as is the case for the spontaneous symmetry breaking [20,21]. Conversely, the ground state of a Hamiltonian may fulfill a symmetry, despite H itself does not, because of other excited states.

Although the existence of a symmetry is per se a "binary" concept –it is either fulfilled or not– one may wonder whether and to what extent the effects of a symmetry breaking become observable. A flux, for instance, breaks time reversal and charge-conjugation symmetries in the Hamiltonian [22,23]. Yet, the rigidity of a band insulator to the flux can also be regarded as an example where the ground state "does not see" these symmetry breaking, and it behaves as if the symmetries were fulfilled. When it comes to out of equilibrium conditions, the effect of symmetries becomes more subtle. It is known,

*fabrizio.dolcini@polito.it

 ©2023 American Physical Society

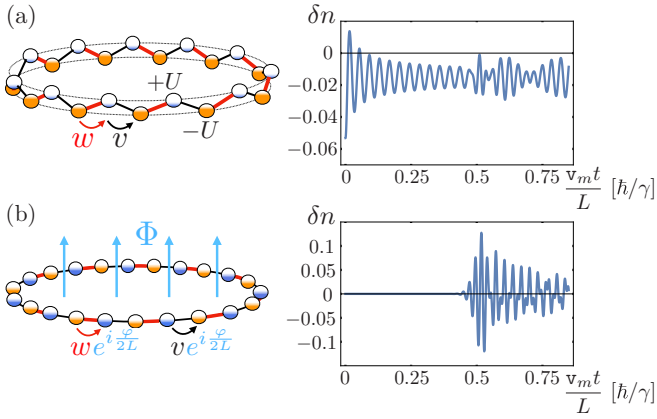

FIG. 1. Quantum dynamics resulting from a quench applied to a dimerized ring-shaped model (14) with $L = 80$ cells (160 sites), where the tunneling amplitudes, with initial values $v^i = 1$ and $w^i = 0.5$, are exchanged $w \leftrightarrow v$. The deviation δn from $1/2$ of the on-site density is shown as a function of time. (a) Case of a staggered potential $U = 1/10$ breaking the charge conjugation symmetry $\mathcal{C}$ locally. (b) Case of a nonlocal $\mathcal{C}$-symmetry breaking induced by a flux phase $\varphi = \pi/2$, where $\varphi = 2\pi\Phi/\Phi_0$, with Φ_0 denoting the flux quantum.

for instance, that a symmetry can get dynamically broken even when it is fulfilled by both the initial state and the evolution Hamiltonian [24,25]. In general terms, one can thus formulate the following problem: When a fermionic system with a broken symmetry is driven far from equilibrium, how and when will the effects of such symmetry breaking become observable?

This paper is devoted to address the above questions. Specifically, focusing on the breaking of the charge-conjugation symmetry $\mathcal{C}$, we analyze the quantum dynamics of a half-filled fermionic model in a 1D ring-shaped dimerized lattice, where a quench in the magnitude of the tunneling amplitudes is performed. We show that, when $\mathcal{C}$ symmetry is broken, the physical behavior at local level crucially depends on (i) the localization properties of the quantum state and (ii) the nature of the symmetry breaking (local *vs* nonlocal). In particular, if the initial state exhibits power-law decay correlations, as is the case of a metal, the effects of $\mathcal{C}$-symmetry breaking emerge at any time, regardless of whether the symmetry is broken locally or nonlocally.

However, if the quantum state is characterized by exponentially decaying correlations, as is the case of an insulator, a twofold scenario can emerge. A local breaking of the $\mathcal{C}$ symmetry straightforwardly impacts on local observables right after the quench. In contrast, if the $\mathcal{C}$ symmetry is broken nonlocally, the expectation values of local observables remain effectively pinned to the unbroken symmetry case for a time that scales linearly with the system size. This result is highlighted in Fig. 1, which shows the dynamical behavior of a half-filled quenched Su-Schrieffer-Heeger (SSH) model [26,27], comparing the cases where $\mathcal{C}$ symmetry is broken locally by an on-site staggered potential [panel (a)], and nonlocally by a magnetic flux [panel (b)]. While in the former case the site density deviates by δn from the uniform half-filled value $1/2$ right after the quench, in the latter scenario the deviation remains exponentially small in the system size L for a time that is proportional to L. Only after such a time, the density starts to wildly deviate from the value $1/2$ and to oscillate. This phenomenon, which we dub tsunami effect, manifests also in the particle current and in the evolution of correlation functions. Notably, such an extensively long time rigidity of these quantities occurs in spite of the chiral symmetry of the SSH model, which gets dynamically broken immediately after the quench, as we quantitatively prove.

These results represent one further step in the exploration of the space-time scaling regime, which investigates the out of equilibrium dynamics for timescales that scale linearly with the system size. While in Ref. [28], this regime was recently shown to provide a new way to topologically classify out of equilibrium quantum systems, the present work highlights that, when an insulator is driven out of equilibrium, the quantum nonlocality induced by a flux becomes observable in such a regime. Indeed, as we shall discuss, the tsunami effect can also be regarded as a *dynamical crossover* characterizing the local density as a function the ratio η between time t and system size L.

The paper is organized as follows. In Sec. II, after briefly recalling the definition and properties of charge conjugation transformation $\mathcal{C}$, we identify in general terms the implications of a $\mathcal{C}$-symmetric many-particle quantum state on the single-particle density matrix. Then, in Sec. III, we specify the two-band model considered here, pointing out the difference between local and nonlocal $\mathcal{C}$-symmetry breaking. Section IV is devoted to the investigation of the dynamics resulting from the quench and to the demonstration of the tsunami effect. In particular, for the SSH ring-shaped lattice threaded by a flux, we show that the local density, current and correlations remain rigid to the nonlocal $\mathcal{C}$-symmetry breaking for an extensively long time. After providing an intuitive explanation of such effect in terms of Wannier functions, in Sec. V, we argue that it can be quantitatively explained by introducing suitable symmetry breaking quantifiers. This enables us to quantitatively distinguish global from local $\mathcal{C}$-symmetry breaking, and also to show that the phenomenon occurs even though the chiral symmetry is dynamically broken immediately after the quench. Moreover, in Sec. VI, we demonstrate the stability of the tsunami effect to weak disorder and interactions. Finally, in Sec. VII, we draw our conclusions and outline some possible experimental realizations to observe the predicted effect.

II. CHARGE CONJUGATION SYMMETRY

Let us consider a system of spinless fermions, possibly interacting or with disorder, in a one-dimensional (1D) ring-shaped lattice with periodic boundary conditions (PBCs). The quantum state of the system, characterized by a many-particle density matrix $\boldsymbol{\rho}$, may be an equilibrium or an out of equilibrium state at a given time t. Without loss of generality, we shall adopt a notation where lattice sites are grouped "in pairs." Each pair, labeled by an integer $j = 1, 2, \ldots, L$, contains an odd and an even site denoted as A and B, respectively, with $c^\dagger_{j\alpha}, c_{j\alpha}$ (with $\alpha = A$ and B) denoting the on-site fermionic creation and annihilation operators, respectively. The reason for choosing this notation is that, although for the moment we shall be quite general, later below we shall focus on dimerized

lattices, and each pair will thus be identified as a cell that is periodically repeated in the lattice.

A. Charge conjugation

Charge conjugation $\mathcal{C}_\theta$ is a linear unitary transformation ($\mathcal{C}_\theta i \mathcal{C}_\theta^\dagger = i$ and $\mathcal{C}_\theta^\dagger = \mathcal{C}_\theta^{-1}$) locally mapping particles into holes as follows [29]:

$$\mathcal{C}_\theta c_{j\alpha}^\dagger \mathcal{C}_\theta^\dagger = (\mathsf{U}_\theta)_{j\alpha;l\beta}\, c_{l\beta}, \tag{1}$$

where a summation over repeated indices is meant, and

$$\mathsf{U}_\theta = \bigoplus_{j=1}^{L} \begin{pmatrix} e^{2i\theta_{jA}} & 0 \\ 0 & -e^{2i\theta_{jB}} \end{pmatrix} \tag{2}$$

is a $2L \times 2L$ block-diagonal matrix in real space, characterized by the set of phases $\{\theta\} = \{\theta_{1A}, \theta_{1B}, \ldots, \theta_{LA}, \theta_{LB}\}$. The minus sign appearing in Eq. (2) for the even ($= B$) sites is purely conventional and can always be included in the θ_{jB} phases.

A many-particle quantum state is charge conjugation symmetric if there exists a choice of the phases $\{\theta\}$ such that the many-particle density matrix operator $\boldsymbol{\rho}$ fulfills $\mathcal{C}_\theta \boldsymbol{\rho} \mathcal{C}_\theta^\dagger = \boldsymbol{\rho}$. To identify the implications of such a symmetry, it is useful to consider the single-particle reduced density matrix, which is the tool needed to compute any one-body expectation value (in particular observables and equal-time correlations), and is defined as

$$\rho_{j_1\alpha_1, j_2\alpha_2} = \langle c_{j_2\alpha_2}^\dagger c_{j_1\alpha_1} \rangle = \mathrm{Tr}\big[\boldsymbol{\rho}\, c_{j_2\alpha_2}^\dagger c_{j_1\alpha_1}\big], \tag{3}$$

with $\alpha_1, \alpha_2 = A, B$. The following general results, whose proof can be found in the Appendix A, hold.

Theorem. If $\mathcal{C}_\theta \boldsymbol{\rho} \mathcal{C}_\theta^\dagger = \boldsymbol{\rho}$ for a set $\{\theta\}$ of phases in. Eq. (1), then

(i) the single-particle reduced density matrix ρ in Eq. (3) fulfills the following property

$$(\rho - \mathbb{I}/2) + \mathsf{U}_\theta^* (\rho^* - \mathbb{I}/2)\, \mathsf{U}_\theta = 0, \tag{4}$$

where U_θ is given by Eq. (2) and $\mathbb{I}$ is the identity in the $2L$-dimensional single-particle Hilbert space. A straightforward implication of Eq. (4), obtained by taking its trace, is that $N = \mathrm{tr}\rho = L$, where N is the number of particles, i.e., *half-filling is a necessary condition for the state* $\boldsymbol{\rho}$ *to be* $\mathcal{C}$*-symmetric*. In order to avoid trivial violations of the $\mathcal{C}$ symmetry, in the rest of our paper we shall thus consider the half-filling situation.

(ii) The expectation value of the local density is

$$\langle n_{j\alpha} \rangle \equiv 1/2 \qquad \forall j, \quad \alpha = A, B. \tag{5}$$

Notice that this is a stronger implication than the overall half-filling condition, for it holds also in the presence of interactions or disorder, where translational invariance is *a priori* broken.

(iii) If an initially $\mathcal{C}$-symmetric quantum state $\boldsymbol{\rho}^i$ evolves according to a $\mathcal{C}$-symmetric Hamiltonian H ($\mathcal{C}_\theta H \mathcal{C}_\theta^\dagger = H$), then the evolved state $\boldsymbol{\rho}(t)$, remains $\mathcal{C}$-symmetric at any time [30]. This is due to the unitarity of $\mathcal{C}$ and implies, in particular, that Eqs. (4) and (5) hold at any time.

$$\langle n_{j\alpha} \rangle(t) \equiv \tfrac{1}{2} \quad \forall j, t \quad \alpha = A, B. \tag{6}$$

In the presence of $\mathcal{C}$ symmetry, the density thus remains pinned to $1/2$ even out of equilibrium. In the following, we shall analyze whether and how Eq. (6) is modified by a $\mathcal{C}$-symmetry breaking.

B. Charge conjugation and gauge transformations

We conclude this section by observing that the matrix (2) characterizing the charge-conjugation transformation (1) can also be rewritten as $\mathsf{U}_\theta = \mathsf{U}_0\, \Lambda_\theta^2$, where

$$\mathsf{U}_0 = \oplus_j \sigma_z \tag{7}$$

is the matrix obtained for $\{0\} = \{\theta_{j\alpha} \equiv 0\ \forall j, \alpha\}$ and

$$\Lambda_\theta = \bigoplus_{j=1}^{L} \begin{pmatrix} e^{i\theta_{jA}} & 0 \\ 0 & e^{i\theta_{jB}} \end{pmatrix}. \tag{8}$$

This means that the charge-conjugation transformation $\mathcal{C}_\theta$ in Eq. (1) can be interpreted as the $\mathcal{C}_0$ transformation

$$\begin{aligned} \mathcal{C}_0\, c_{jA}^\dagger\, \mathcal{C}_0^\dagger &= +c_{jA} \\ \mathcal{C}_0\, c_{jB}^\dagger\, \mathcal{C}_0^\dagger &= -c_{jB} \end{aligned}, \tag{9}$$

combined with a local gauge transformation on the fermionic operators [31]

$$c_{j\alpha}^\dagger = e^{i\theta_{j\alpha}} \tilde{c}_{j\alpha}^\dagger, \tag{10}$$

which is compactly written as

$$[0] \overset{\{\theta\}}{\to} [g], \tag{11}$$

where [0] denotes the original gauge of the $c^\dagger$ operators and $[g]$ the new gauge of the $\tilde{c}^\dagger$ operators. As a consequence of Eq. (10), the entries of the single-particle density matrix (3) also change by such phase factors,

$$\rho \ \to \ \rho(\{\theta\}) = \Lambda_\theta \rho \Lambda_\theta^*. \tag{12}$$

One can thus reformulate the above theorem as follows. If a quantum state $\boldsymbol{\rho}$ is charge-conjugation symmetric for a phase set $\{\theta\}$, then by performing the local gauge transformation (10) and (11) the single-particle density matrix $\rho(\{\theta\})$ in the $\tilde{c}^\dagger$ basis fulfills

$$[\rho(\{\theta\}) - \mathbb{I}/2] + \mathsf{U}_0\, [\rho^*(\{\theta\}) - \mathbb{I}/2]\, \mathsf{U}_0 = 0. \tag{13}$$

In other words, one can equivalently define the charge conjugation transformation only as $\mathcal{C}_0$ in Eq. (9), provided that the possibility to perform gauge transformations (10) is also included. This is because the $\mathcal{C}_0$ symmetry may be present in the state but hidden by an inappropriate choice of the gauge.

Since expectation values of observables are independent of the choice of the gauge, in the following of the paper we shall often harness this interpretation in terms of gauge transformations.

III. MODEL, LOCAL VersuS NONLOCAL $\mathcal{C}$-SYMMETRY BREAKING

A. The model

So far, the above statements have been quite general. In order to illustrate their applications we shall focus on a

specific model in a dimerized lattice with PBCs, described by the following Hamiltonian

$$H = \gamma \left[\sum_{j=1}^{L} \left(v\, e^{i\frac{\varphi}{2L}} c^{\dagger}_{jA} c_{jB} + w\, e^{i\frac{\varphi}{2L}} c^{\dagger}_{jB} c_{j+1A} + \text{H.c.} \right) + \right. \\ \left. + U \sum_{j=1}^{L} (n_{jA} - n_{jB}) \right]. \tag{14}$$

The first line in Eq. (14) is the SSH model [26,27], where γ is an energy scale unit related to the bandwidth, v and w are the (real) dimensionless intracell and intercell hopping amplitudes, respectively, while $\varphi = 2\pi\,\Phi/\Phi_0$ is the phase related to the magnetic flux Φ threading the ring, in units of the flux quantum Φ_0. The second line describes an on-site staggered potential U in the two cell sites, in units of γ. For $U \neq 0$, the full model (14) is known as the Rice-Mele (RM) model [32].

Let us recall a few aspects of the model Eq. (14) that will be necessary to illustrate the gist of the tsunami effect. Exploiting the cell translational invariance, the Hamiltonian (14) can be suitably rewritten in momentum space as

$$H[\phi] = \gamma \sum_{k=-\pi}^{\pi} (c^{\dagger}_{kA}, c^{\dagger}_{kB})\, \mathbf{d}(k) \cdot \boldsymbol{\sigma} \begin{pmatrix} c_{kA} \\ c_{kB} \end{pmatrix}, \tag{15}$$

where the k wave vectors, here measured in units of the inverse cell size, are quantized as $k = 2\pi\, n/L$, where $n \in \{-\lfloor L/2 \rfloor, \ldots, \lfloor (L-1)/2 \rfloor\}$. Moreover $\boldsymbol{\sigma} = (\sigma_x, \sigma_y, \sigma_z)$ are Pauli matrices acting on the sublattice degree of freedom, and

$$\mathbf{d}(k) = \left(v \cos\frac{\varphi}{2L} + w \cos\left(k + \frac{\varphi}{2L}\right), \right. \\ \left. - v \sin\frac{\varphi}{2L} + w \sin\left(k + \frac{\varphi}{2L}\right), U \right) \tag{16}$$

denotes the vector field along the Brillouin zone. The spectrum consists of two bands $E_{\pm}(k) = \gamma \varepsilon_{\pm}(k)$, where the dimensionless dispersion relations $\varepsilon_{\pm}(k) = \pm|\mathbf{d}(k)|$ explicitly read

$$\varepsilon_{\pm}(k) = \pm \sqrt{v^2 + w^2 + 2vw \cos\left(k + \frac{\varphi}{L}\right) + U^2}. \tag{17}$$

As is well known, the spectrum (17) is gapped in the presence of either dimerization ($v \neq w$) or on-site staggered potential ($U \neq 0$), and gapless otherwise, while the flux phase φ leads to a shift in the momenta. The quantity $\mathsf{v}_m = \max[\partial_k \varepsilon(k)]$ identifying the maximal (dimensionless) group velocity characterizing the excitations along the ring is given by

$$\mathsf{v}_m = \sqrt{\frac{\mathsf{A} - \sqrt{\mathsf{A}^2 - \mathsf{B}^2}}{2}}, \tag{18}$$

where $\mathsf{A} = v^2 + w^2 + U^2$ and $\mathsf{B} = 2vw$. The single-particle eigenstates $|k, \pm\rangle = |k\rangle \otimes |u_{\pm}(k)\rangle$ are determined through the eigenvalue problem $(\hat{\mathbf{d}}(k) \cdot \boldsymbol{\sigma})|u_{\pm}(k)\rangle = \pm|u_{\pm}(k)\rangle$, where $\hat{\mathbf{d}}(k) = \mathbf{d}(k)/|\mathbf{d}(k)|$ is the unit vector field.

In the SSH model ($U = 0$), the two regimes $v > w$ and $v < w$ are known to identify two topologically distinct insulators [33].

B. Local versus nonlocal $\mathcal{C}$-symmetry breaking

Similarly to a quantum state $\boldsymbol{\rho}$, a Hamiltonian H is charge conjugation symmetric if there exists a set $\{\theta\}$ of phases such that $\mathcal{C}_\theta H \mathcal{C}_\theta^{\dagger} = H$. On account of the above discussion about gauge transformations, one can equivalently say that H is charge conjugation symmetric if there exists a gauge transformation (10) such that $\mathcal{C}_0 H(\{\theta\})\mathcal{C}_0^{\dagger} = H(\{\theta\})$, where $H(\{\theta\})$ is the Hamiltonian H re-expressed as a function of the gauge operators $\tilde{c}_{j\alpha}$, $\tilde{c}^{\dagger}_{j\alpha}$.

It is straightforward to verify that the Hamiltonian (14) *does not* exhibit charge conjugation-symmetry, unless $U = 0$ and $\varphi = m\pi$. In particular, one can observe that the $\mathcal{C}$ symmetry is broken *locally* by the on-site potential $U \neq 0$. Indeed, for any site (j, α), the projection

$$H_{j\alpha} = \mathcal{P}_{j\alpha} H \mathcal{P}_{j\alpha} \tag{19}$$

of the Hamiltonian on that site always fulfills $H_{j\alpha} - \mathcal{C}_\theta H_{j\alpha} \mathcal{C}_\theta^{\dagger} \neq 0$, for all choices of the $\{\theta\}$ phases in Eq. (1). Equivalently, there is no gauge transformation (10) that can remove the $\mathcal{C}$-breaking potential U present in that site (j, α).

In contrast, the presence of the flux phase $\varphi \neq m\pi$ breaks $\mathcal{C}$ *nonlocally*, meaning that for any fixed local portion P of the ring there is always a phase set $\{\theta\}$ leading to $H_P - \mathcal{C}_\theta H_P \mathcal{C}_\theta^{\dagger} = 0$, where $H_P = \mathcal{P}_P H \mathcal{P}_P$ is the Hamiltonian projected on that portion. For instance, by choosing the following set of linearly growing phases,

$$\{\theta_\ell\} \equiv \begin{cases} \theta_{j,A} = \frac{\varphi}{L}\,(j - \frac{1}{4}) \\ \theta_{j,B} = \frac{\varphi}{L}\,(j + \frac{1}{4}) \end{cases} \qquad j = 1, , \ldots, L\ , \tag{20}$$

the $\mathcal{C}$ symmetry is realized almost everywhere in the ring, except in the link between sites (L, B) and $(1, A)$, where $\mathcal{C}$ symmetry is broken [34]. In other words, the gauge transformation (10) with phases (20) accumulates the entire flux phase in such link. Similar phase choices accumulate the $\mathcal{C}$-breaking elsewhere. Note that the possibility of performing the gauge transformation is the reason why the model Eq. (14), when defined in a lattice with *open* boundary conditions (OBCs), i.e., on a chain, is $\mathcal{C}$-symmetric. Indeed, since a chain can be regarded as a ring with one missing link, it is always possible to get rid of the phase φ appearing in the tunneling amplitudes by "accumulating" it along such a link. In contrast, in the ring-shaped geometry considered here, the PBCs imply that $H - \mathcal{C}_\theta H \mathcal{C}_\theta^{\dagger} = 0$ cannot be realized in all links, and at least one $\mathcal{C}$-breaking link will always be present for topological reasons.

IV. TSUNAMI EFFECT

A. $\mathcal{C}$-symmetry breaking for the ground state

We start from some preliminary analysis at equilibrium. When the Hamiltonian (14) fulfills the $\mathcal{C}$ symmetry ($U = 0$ and $\varphi = \pi m$), its nondegenerate ground state at half filling also does. If the $\mathcal{C}$ symmetry of the Hamiltonian is explicitly broken by $U \neq 0$ or $\varphi \neq \pi m$, this will reflect on its ground state. In particular, because of the dimerization, one expects the density to deviate from Eq. (5) and to acquire the form

$$n_{A/B} = \langle n_{j,A/B} \rangle = \tfrac{1}{2} \pm \delta n \qquad \forall j, \tag{21}$$

where the deviation δn, which represents the sublattice unbalance, is independent of the cell j because of the cell translational invariance of model (14).

However, for $U = 0$, i.e., in the SSH model, Eq. (5) still holds strictly for any length L, despite the $\mathcal{C}$-breaking flux φ. The reason is that such a model exhibits the additional chiral symmetry $\mathcal{S}$ [33], which forbids deviations from Eq. (5) for the ground state, even in the presence of the flux [30]. This can be explicitly seen from the general expression

$$\delta n = -\frac{1}{2L}\sum_{k=-\pi}^{\pi} \hat{d}_z(k), \tag{22}$$

where $\hat{d}_z(k)$ is the z component of the unit vector related to $\mathbf{d}(k)$ in Eq. (16), and vanishes in the SSH model. In contrast, in the RM model, the staggered on-site potential $U \neq 0$ does lead to a deviation δn in Eq. (21), which in the thermodynamic limit reads

$$\delta n = -\frac{1}{\pi}\frac{U}{\sqrt{U^2+(v+w)^2}}\mathsf{K}\left(\frac{4vw}{U^2+(v+w)^2}\right), \tag{23}$$

where K is the complete elliptic integral of the first kind.

B. Quench dynamics

While at equilibrium the effects of $\mathcal{C}$-breaking induced by the flux may be masked by the additional chiral symmetry $\mathcal{S}$, when the system is driven out of equilibrium such a symmetry gets broken *dynamically* because of its antiunitary character [24,25], and its protection is lost in the dynamically evolving quantum state. At first, one can thus expect deviations from Eq. (5) to emerge also in the SSH model right after the quench. As we shall see, this is not the case, though. Let us thus analyze a quantum quench protocol, where the system is initially prepared in the ground state $\boldsymbol{\rho}^i$ of some initial (prequench) Hamiltonian H^i. At $t = 0$, the Hamiltonian parameters are suddenly changed ($H^i \to H^f$), so that the dynamical evolution $\boldsymbol{\rho}(t) = \exp[-iH^f t/\hbar]\boldsymbol{\rho}^i \exp[+iH^f t/\hbar]$ is governed by the postquench Hamiltonian H^f. We denote by $\mathbf{d}^i(k)$ and $\mathbf{d}^f(k)$ the vector fields characterizing H^i and H^f, respectively, in Eq. (15). As motivated in Introduction, the $\mathcal{C}$-breaking parameters, namely the flux phase φ and the local on-site potential U, will be kept constant across the quench. We shall mainly focus here on the quench protocol that exchanges the hopping amplitudes, i.e.,

$$\begin{array}{ccc} v^i = 1 & \to & v^f = r, \\ w^i = r & \to & w^f = 1, \end{array} \tag{24}$$

where r is a dimensionless parameter characterizing the dimerization strength ($0 < r < 1$). The cases of other quench protocols will be addressed later. For the sake of completeness, before presenting the results, a few technical details are in order. The initial single-particle density matrix describing the ground state of H^i with its fully occupied lower band is block-diagonal in k space, $\rho^i = \oplus_k \rho^i(k)$, where $\rho^i(k) = |u^i_-(k)\rangle\langle u^i_-(k)| = (\sigma_0 - \hat{\mathbf{d}}^i(k)\cdot\boldsymbol{\sigma})/2$, σ_0 denotes the 2×2 identity matrix, and $\hat{\mathbf{d}}^i(k) = \mathbf{d}^i(k)/|\mathbf{d}^i(k)|$ is the initial unit vector field. Because the quench dynamics is decoupled is k space, the k block of the evolved density matrix is $\rho_-(k,t) = |u_-(k,t)\rangle\langle u_-(k,t)|$, where $|u_-(k,t)\rangle = \exp[-i\mathbf{d}^f(k)\cdot\boldsymbol{\sigma}\gamma t/\hbar]|u^i_-(k)\rangle$, and can always be written as $\rho_-(k,t) = [\sigma_0 - \hat{\mathbf{d}}(k,t)\cdot\boldsymbol{\sigma}]/2$, where $\hat{\mathbf{d}}(k,t)$ is a time-dependent unit vector given by [35]

$$\begin{aligned}\hat{\mathbf{d}}(k,t) = {}& \mathbf{d}_\parallel(k) + \mathbf{d}_\perp(k)\cos[2|\mathbf{d}^f(k)|\tau] \\ & + \mathbf{d}_\times(k)\sin[2|\mathbf{d}^f(k)|\tau],\end{aligned} \tag{25}$$

where $\mathbf{d}_\parallel(k) = [\hat{\mathbf{d}}^i(k)\cdot\hat{\mathbf{d}}^f(k)]\hat{\mathbf{d}}^f(k)$, $\mathbf{d}_\perp(k) = \hat{\mathbf{d}}^i(k) - \mathbf{d}_\parallel(k)$, and $\mathbf{d}_\times(k) = -[\hat{\mathbf{d}}^i(k)\times\hat{\mathbf{d}}^f(k)]$, with $\hat{\mathbf{d}}^f(k) = \mathbf{d}^f(k)/|\mathbf{d}^f(k)|$, and

$$\tau = \frac{t\,\gamma}{\hbar} \tag{26}$$

denotes the dimensionless time.

The knowledge of the single-particle density matrix ρ, when rewritten in real space through $\rho_{j_1\alpha_1,j_2\alpha_2}(t) = L^{-1}\sum_k e^{ik(j_1-j_2)}(\rho_-)_{\alpha_1\alpha_2}(k,t)$ [see Eq. (3)], straightforwardly provides the dynamical evolution of the site density expectation value (diagonal entries) and all two-point correlations (off-diagonal entries). Here below we shall illustrate the dynamical behavior of these quantities.

1. On-site density and currents

Density. Even far from equilibrium, the cell translational invariance enables us to write the on-site density as $n_{A/B}(t) = 1/2 \pm \delta n(t)$, and it is thus sufficient to analyze the dynamical behavior of the deviation $\delta n(t)$, which is independent of the cell j. We recall that, if the $\mathcal{C}$ symmetry were fulfilled by the initial state and by the Hamiltonian, i.e., if $U = 0$ and $\varphi = 0$, the density would be pinned to $1/2$ [see Eq. (6)] and the deviation would be strictly vanishing at any time, $\delta n(t) \equiv 0$. In the case of the RM model without flux ($\varphi = 0$), where the $\mathcal{C}$-symmetry breaking is induced locally by the on-site staggered potential $U \neq 0$, the deviation is already nonvanishing in the prequench state, and after the quench it significantly fluctuates in time, as displayed in Fig. 1(a). In contrast, in the SSH model ($U = 0$), where $\mathcal{C}$ symmetry is broken nonlocally by the presence of a flux φ, the density remains effectively pinned to $1/2$ for a strikingly long time, proportional to the system size L, after which the deviation starts to appreciably fluctuate [see Fig. 1(b)]. This is the tsunami effect arising from quantum dynamics. In order to gain more quantitative information, we have investigated the limit of a strongly dimerized ring ($r \ll 1$), where it is possible to find an analytical expression for the density behavior in the considered quench protocol (24). In particular, for even L, one has

$$\delta n(\tau) \simeq \frac{L}{2\tau\, r}(-1)^{\frac{L+2}{2}} J_L(2\tau r)\,\cos(2\tau)\sin\varphi, \tag{27}$$

with J_L denoting the Bessel function of order L. A similar expression can be obtained for odd L (see Appendix B). Equation (27) holds for times $2\tau r < 2L$, as can be seen from Fig. 2, where we have compared the exact numerical evolution (solid blue curve) with the asymptotic approximation (dashed red curve), for a dimerization $r = 0.1$. While technical details of such derivation can be found in Appendix B, here we emphasize the insights gained from Eq. (27). First, the flux determines the maximal magnitude of density deviation, which vanish in the $\mathcal{C}$-symmetric case ($\varphi = \pi m$), as expected, and are maximal for $\varphi = \pi(m + 1/2)$ with $m \in \mathbb{Z}$. Second,

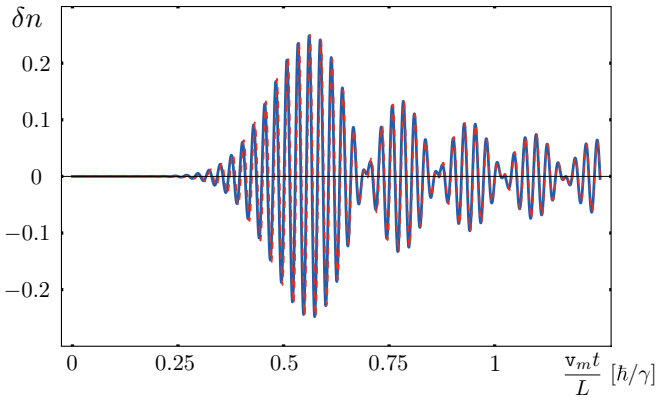

FIG. 2. Time evolution of the on-site density deviation [see Eq. (21)] in a SSH ring with $L = 12$ cells (=24 sites), threaded by a magnetic flux $\varphi = \pi/2$, undergoing the quench protocol (24), with dimerization $r = 0.1$. The analytical expression (27) obtained in the strongly dimerized limit (red dashed curve) perfectly reproduces the numerically exact evolution (blue curve). The deviation δn is exponentially small in the system size L [see Eq. (28)] for an extensively long time.

the asymptotic expansion of the Bessel function shows that for the time range $2\tau r \ll \sqrt{L}$, one has

$$\delta n(\tau) \simeq \left(\frac{\tau r e}{L}\right)^L, \tag{28}$$

i.e., the deviations from $1/2$ are suppressed *exponentially* with the system size L, whereas for longer time $L \lesssim 2\tau r < 2L$ the deviation $\delta n(\tau)$ acquires a double period structure, namely, a longer period envelope function $J_L(2\tau r) \sim \cos(2\tau r - \pi/4)/\sqrt{\pi \tau r}$, characterized by an *algebraic* decay, multiplied by the shorter period oscillatory function $\cos(2\tau)$. Finally, by noticing that in the SSH model the maximal velocity (18) reduces to $\mathrm{v}_m = w = r$, the time

$$\tau_2^* = \frac{L}{2r} = \frac{L}{2\mathrm{v}_m} \tag{29}$$

represents an estimate of the onset of the tsunami effect, i.e., the time characterizing a dynamical crossover between the exponential and the algebraic suppression in L of the density deviation δn. Roughly, the onset time τ_2^* also represents the time, at which δn reaches its first maximal value. As one can see from Eq. (29), τ_2^* grows linearly with the system size L while, at fixed L, it increases for lower values r, i.e., for stronger dimerization.

We emphasize that, while for the specific protocol (24) it is possible to gain the analytical expression Eq. (27) for the density dynamics, the occurrence of the tsunami effect is by no means restricted to such case. A qualitatively very similar result emerges both if the quench is performed across the two topologically distinct phases and within the same topological phase, and also when hopping terms between next-to-nearest neighbor cells are included. While the magnitude of the density deviation δn after the tsunami onset quantitatively depends on the specific values of the prequench and postquench parameters, the tsunami effect is a quite generic phenomenon occurring for any quench, provided that the $\mathcal{C}$ symmetry is broken nonlocally by the flux and the initial state is insulating ($v^i \neq w^i$).

The importance of an initially insulating state for the tsunami effect can be understood by comparing the dynamical density behavior in the case where the initial state is the half-filled ground state of the nondimerized Hamiltonian H^i with flux, i.e., a metallic ground state. By performing a quench to a dimerized H^f through the protocol

$$\begin{aligned} v^i = 1 \quad &\rightarrow \quad v^f = 1, \\ w^i = 1 \quad &\rightarrow \quad w^f = r, \end{aligned} \tag{30}$$

one obtains a density deviation emerging immediately after the quench, and scaling as $O(1/L)$. Indeed, already for short times $\tau \ll L/\mathrm{v}_m$ and small flux $0 < \varphi \ll \pi/2$, one can find for odd L

$$\delta n(\tau) \simeq -\frac{\sin[2(1-r)\tau]}{\pi} \frac{\varphi}{2L} \tag{31}$$

indicating that no tsunami effect is present for an initially metallic state. A similar formula is found for even L.

Currents. When the tsunami effect starts to manifest itself in the SSH model (see Fig. 2), the densities in sites A and B of each cell start to fluctuate oppositely, $n_{A/B}(t) = 1/2 \pm \delta n(t)$. These fluctuations represent oscillating dipoles, which in turn generate nonstationary currents. Specifically, in a dimerized lattice one has intercell and intracell particle currents, given by

$$\hat{J}_j^{\mathrm{inter}} = \frac{\gamma}{\hbar} w \left(i e^{i\frac{\varphi}{2L}} c_{jB}^\dagger c_{j+1A} - i e^{-i\frac{\varphi}{2L}} c_{j+1A}^\dagger c_{jB} \right) \tag{32}$$

and

$$\hat{J}_j^{\mathrm{intra}} = \frac{\gamma}{\hbar} v \left(i e^{i\frac{\varphi}{2L}} c_{jA}^\dagger c_{jB} - i e^{-i\frac{\varphi}{2L}} c_{jB}^\dagger c_{jA} \right), \tag{33}$$

respectively. Their expectation values can be computed by exploiting the cell translational invariance

$$J^\nu = \frac{1}{L} \sum_{j=1}^{L} \langle \hat{J}_j^\nu \rangle \quad \nu = \mathrm{inter/intra} \tag{34}$$

and by means of the single-particle density matrix (3). From the continuity equation $\partial_t(\delta n) = J^{\mathrm{inter}} - J^{\mathrm{intra}}$, one can straightforwardly deduce that the tsunami effect characterizing δn is also present in the currents (plots not shown here).

2. Correlations

The off-diagonal entries of the single-particle density matrix (3) describe the two-point equal time correlation functions, which only depend on the relative distance l between two cells, due to cell translational invariance. For definiteness, we have taken L to be even and, focusing on the "central" cell $j^* = L/2$ as a reference cell, we have analyzed its correlation $\rho_{L/2+l,\alpha;L/2,\beta}(t)$ with any other cell located at an arbitrary distance $l \in [-L/2+1, L/2]$ from j^*, with $\alpha, \beta = A, B$. We want to investigate when the presence of the magnetic flux manifests itself in correlations.

Let $P^* = (j^*, A)$ denote a reference point, namely, the A-site of the reference cell, and $P = (j^* + l, A)$ another A site, as depicted by the red and black dots in Fig. 3(a), respectively. As a result of the quench, excitations emerging from the midpoint (grey dot) between P^* and P start to propagate in

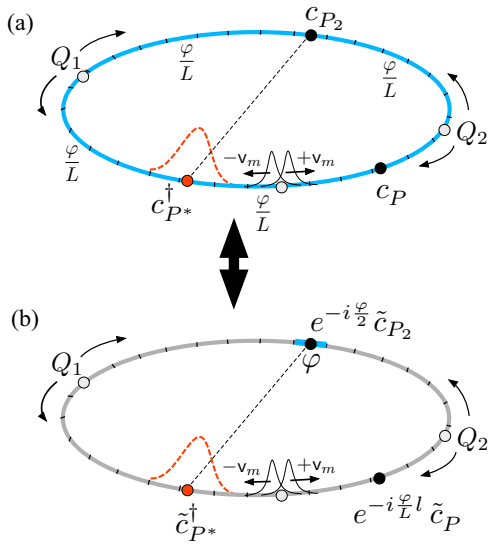

FIG. 3. Correlations between the reference point P^* (red dot) and any other point P along the ring (black dots) evolve in time, as a result of the quench because pairs of counter-propagating excitations depart from intermediate ring points (grey dots) and reach the envisaged red and black points. The nonlocal presence of the flux can be observed only when two pairs of excitations, departed from intermediate points Q_1 and Q_2, have covered the *entire* ring and have reached the two points (red and black) simultaneously. The two panels illustrate two types of gauges describing the presence of the magnetic flux threading the ring. (a) The flux phase φ is uniformly distributed along the ring, so that the vector potential along each link is $O(\varphi/L)$. (b) The flux phase φ is accumulated only along the link located oppositely to the reference point P^*.

opposite directions, with typical group velocities $\pm v_m$ of the postquench Hamiltonian H^f [see Eq. (18)], and reach at the same time the two points P^* and P, which thus get correlated. We emphasize that, although these excitations traveling along the ring arc see the local phase φ/L across each cell (depicted in blue in Fig. 3), this cannot encode the nonlocal effect of the flux. Indeed, at such time these excitations have only traveled a *portion* of the ring and cannot distinguish a chain with OBCs, which is $\mathcal{C}$-symmetric, from a ring with PBCs threaded by flux that breaks $\mathcal{C}$ symmetry. The presence of the flux can manifest itself only after excitations have explored the *entire* ring. At a more formal level, this can be seen by applying the gauge transformation (10) with Eq. (20), which removes the tunneling amplitude complex phases from almost all links in the Hamiltonian (14) and accumulates the entire flux phase φ along the link opposite to the reference point P^*, as shown by the blue link at P_2 in Fig. 3(b). In this way, the correlation function between (say) A sites is rewritten as

$$\rho_{\frac{L}{2}+l,A;\frac{L}{2},A} = \langle c^\dagger_{\frac{L}{2},A} c_{\frac{L}{2}+l,A}\rangle = e^{-i\frac{\varphi}{L}l}\tilde{\rho}_{\frac{L}{2}+lA,\frac{L}{2}A}, \tag{35}$$

where $e^{-i\frac{\varphi}{L}l}$ is a trivial time-independent phase factor, while $\tilde{\rho}_{L/2+lA;L/2,A} = \langle \tilde{c}^\dagger_{L/2,A}\tilde{c}_{L/2+l,A}\rangle$ is the correlation in the new gauge.

Such a new gauge enables us to highlight the crucial role of the localization properties of the quantum state. Indeed, if the correlation term $\tilde{\rho}_{L/2+lA;L/2,A}$ in Eq. (35) has a quasilong range, i.e., a spatially slow power law decay in l, as is the case in a metal, the reference point P^* does feel the presence of the flux accumulated at the opposite site P_2 of the ring, even in the initial prequench state. In contrast, if the state is characterized by exponentially decaying correlations, as is the case in an insulator, $\tilde{\rho}_{L/2+lA;L/2,A}$ is initially independent of φ, and the flux phase in P_2 remains invisible to P^*. In order to analyze when a nontrivial flux dependence emerges in an insulator, we have thus first singled out the trivial phase factor in Eq. (35) and then subtracted the correlations in the absence of flux. Explicitly, the quantity

$$\Delta\rho_{\frac{L}{2}+l,\alpha_2;\frac{L}{2},\alpha_1} \doteq \tilde{\rho}_{\frac{L}{2}+l,\alpha_2;\frac{L}{2},\alpha_1}\Big|_{\varphi\neq 0} - \rho_{\frac{L}{2}+l,\alpha_2;\frac{L}{2},\alpha_1}\Big|_{\varphi=0} \tag{36}$$

encodes the nontrivial dynamical effects of the flux on the quenched system. In Fig. 4(a), we have plotted $|\Delta\rho|$ of Eq. (36) for $\alpha_1 = \alpha_2 = A$ as a function of time and cell distance l, in a quenched SSH model of $L = 80$ cells (=160 sites), with dimerization parameter $r = 0.7$, and flux phase $\varphi = \pi/4$. The plot shows that the tsunami effect is present also in the correlations, since the difference $\Delta\rho$ from the zero-flux case is vanishing until the extensive time

$$\tau_1^* = \frac{L}{4v_m}, \tag{37}$$

when a $\Delta\rho \neq 0$ starts to be visible at the maximal distance $l = \pm L/2 = \pm 40$. Only after τ_1^* a nontrivial flux dependence arises between the red reference point P^* and the black point P_2 located symmetrically with respect to it (see Fig. 3). The time (37), highlighted in Fig. 4 by a vertical red dashed line, can be interpreted as the time when two pairs of counter-propagating excitations departing after the quench from the points Q_1 and Q_2 (grey dots) simultaneously reach P^* and P_2, after traveling a distance $L/4$ each, thereby covering the entire ring and probing the presence of the flux. This time is of course independent of the chosen gauge (a) or (b) in Fig. 3.

After the time τ_1^*, the correlation $\Delta\rho$ dynamically propagates along the ring following two symmetrical light-cone trajectories in space time [blue lines in Fig. 4(a)], characterized by a velocity $2v_m$ resulting from the pair of counter-propagating excitations traveling at $\pm v_m$. These light cones intersect at distance $l = 0$ at the time τ_2^* given by Eq. (29), as highlighted by a vertical black dashed line. Notice that the A-A correlation difference $\Delta\rho$ at "zero distance" ($l = 0$) is nothing but the on-site density deviation $\delta n = \langle n_{L/2,A}\rangle - \langle n_{L/2,A}\rangle|_{\varphi=0}$. This is shown in Fig. 4(b), which represents a cut at $l = 0$ of the correlation plot displayed in panel (a). Notably, the time τ_1^* in Eq. (37) is a half of the time τ_2^* in Eq. (29). This is because a nonlocal effect such as the presence of the flux impacts on nonlocal correlations *earlier* than the local density, which thus experiences the tsunami effect onset as last. Indeed, referring to Fig. 3, the density in P^* can be considered as the correlation between P^* and $P \equiv P^*$, and the effect of the flux can only appear when a pair of counter-propagating excitations departing from the point P_2 have traveled a distance $L/2$ each, thereby probing the flux presence over the entire ring.

Correlation lightcones then continue to evolve in the ring space-time as shown in Fig. 4(a), where the bottom and top are identified simply because of the PBCs. Notice that crossings at minimal distance $l = 0$ always occur at times

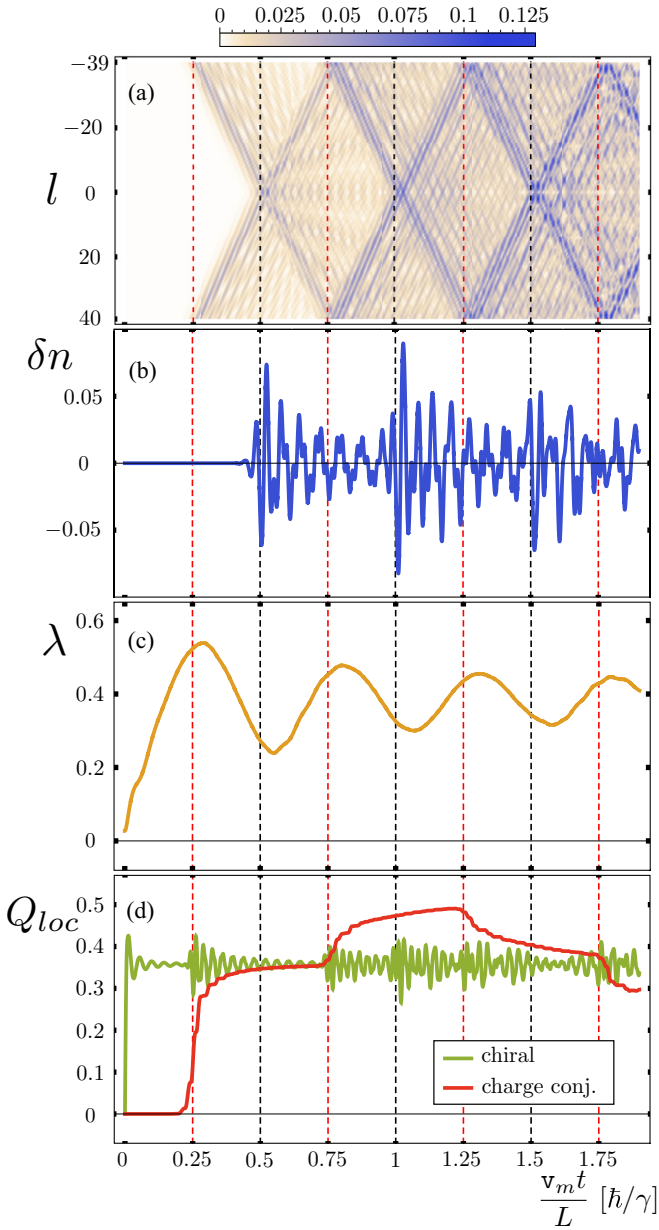

FIG. 4. Dynamics of the SSH ring [Eq. (14) with $U = 0$], with $L = 80$ cells ($= 160$ sites), threaded by a flux ($\varphi = \pi/4$), quenched with the protocol (24), with dimerization parameter $r = 0.7$. (a) density plot of the space-time behavior of correlations, with $l \in [-L/2, L/2]$ denoting the distance between two sites. (b) The dynamical behavior of the site density deviation δn from $1/2$ [see Eq. (21)]. (c) The time evolution of the maximally localized Wannier functions. (d) Time-evolution of the quantifiers of local breaking for chiral symmetry (green curve) and charge-conjugation symmetry (red curve).

$\tau^*_{2n} = 2n\tau^*_1 = n\tau^*_2$, as highlighted by the black vertical dashed lines, and roughly correspond to the maximal peaks of the density shown in Fig. 4(b). Similarly, correlations at maximal distance $l = \pm L/2$ always occur at times $\tau^*_{2n+1} = (2n+1)\tau^*_1 = (n+1/2)\tau^*_2$, as highlighted by the red vertical dashed lines. At very long times, one observes that light cones start to become less sharp, due to the dispersion related to the band curvature.

3. *Wannier localization length*

We have thus seen that, when the $\mathcal{C}$ symmetry is broken, the dynamical response to a quench dramatically depends on whether the symmetry is broken locally, like in the RM model ($U \neq 0$), or nonlocally, like in the SSH model with flux ($\varphi \neq 0$). In particular, in the latter case the local observables and correlations appear effectively robust to the $\mathcal{C}$-breaking and behave as if $\mathcal{C}$ symmetry were preserved for an extensively long time, as shown in Figs. 1 and 4. Here we would like to interpret this effect in terms of Wannier functions. Indeed we recall that the ground state of a band insulator can always be considered as a Slater determinant of Wannier functions, localized around the various lattice cells. In particular it is possible to identify maximally localized Wannier functions (MLWFs), whose spread provides the physical localization length of the system. While in the thermodynamic limit ($L \to \infty$), the definition of MLWFs is well established [36–39], in the case of finite size systems with PBCs analyzed here, their derivation requires some care. However, this can be done by harnessing concepts of directional statistics [40], and an angular localization length λ can be identified in the ring (details of this derivation are given in Appendix C). This quantity enables us to understand the difference between the local *vs* nonlocal $\mathcal{C}$-symmetry breaking. Indeed, in the RM insulator, a localized function is directly affected by a local potential $U \neq 0$ present within its localization length. In contrast, in the SSH insulator, a Wannier function cannot be sensibly affected by the flux φ, which requires to probe the entire ring. This is clearly seen by invoking again the gauge transformation illustrated in Fig. 3(b), where the Wannier function centered around the reference point P (sketched as a red dashed Gaussian curve) cannot "see" the flux accumulated on the other side of the ring. In contrast, in a metal, where Wannier functions are delocalized, namely algebraically decaying in space [36–39], the nonlocal $\mathcal{C}$-symmetry breaking due to the flux can be felt by the ground state.

Focussing now on the SSH model, we have also determined the dynamical evolution of the MLWF localization length λ after the quench. The result is displayed in Fig. 4(c) and shows that λ starts to increase after the quench. We recall that the Wannier (angular) localization length λ also determines the typical lengthscale, over which two ring cells are correlated. Thus the lightcones shown in Fig. 4(a) and describing the evolution of correlations in space-time can also be seen as the dynamical spreading of the Wannier localization length λ.

The increase of λ reaches a maximal value roughly at the time τ^*_1. By comparing with Fig. 4(a), we recall that τ^*_1 is the time when the tsunami effect appears for the very first time, and it occurs in the correlation length of two maximally separated points ($l = \pm L/2$), as highlighted by the red dashed vertical line in Fig. 4. This means that τ^*_1 corresponds to the time where the Wannier functions have widespread enough to explore the entire ring and to probe the existence of the flux. A closer inspection shows that the maximum of the Wannier spreading actually occurs with a slight delay with respect to τ^*_1. This is due to the fact that, because of the curvature of the band dispersion relation, excitations do not all propagate at the same velocity, as is also clear from the color fringes in Fig. 4(a). Thus, while τ^*_1 corresponds to the earliest arrival

of the counter-propagating excitations traveling with maximal velocity v_m, the maximal spreading of the Wannier function occurs when also slowlier excitations have traveled the distance $L/2$.

After reaching the maximum, the localization length λ decreases and reaches a local minimum roughly at time τ_2^*, which is the latest time when the tsunami effect manifests itself, and it occurs at the minimal distance correlation ($l = 0$), namely the on-site density [see Fig. 4(b), and black dashed vertical lines]. After such time, $\lambda(t)$ exhibits an oscillatory behavior, where minima and maxima roughly occur at the times τ_{2n}^* and τ_{2n+1}^*, respectively, up to the delays originating from the band curvature.

4. *Charge conjugation* vs *chiral symmetry breaking*

Before concluding this section, a remark is in order about the different impact of charge conjugation and chiral symmetries at local level. We recall that the chiral transformation $\mathcal{S}$ is an antiunitary transformation ($\mathcal{S}i\mathcal{S}^\dagger = -i$ and $\mathcal{S}^\dagger = \mathcal{S}^{-1}$), whose action

$$\begin{aligned} \mathcal{S}c_{jA}^\dagger\mathcal{S}^\dagger &= +c_{jA} \\ \mathcal{S}c_{jB}^\dagger\mathcal{S}^\dagger &= -c_{jB} \end{aligned} \tag{38}$$

can be compactly written as

$$\mathcal{S}c_{j\alpha}^\dagger\mathcal{S}^\dagger = (\mathsf{U}_0)_{j\alpha;l\beta}\, c_{l\beta}, \tag{39}$$

where U_0 is given in Eq. (7). Notice that, differently from $\mathcal{C}$, the action of $\mathcal{S}$ is unaffected by a gauge transformation (10), due to its antilinear character.

The SSH Hamiltonian $H_{\rm SSH}$ [i.e., Eq. (14) with $U = 0$] is known to fulfill the chiral symmetry [33] ($\mathcal{S}H_{\rm SSH}\mathcal{S}^\dagger = H_{\rm SSH}$) and so does its ground state, even in the presence of a magnetic flux. Thus, at equilibrium the presence of the chiral symmetry $\mathcal{S}$ forces the local density to equal $1/2$ in each site, thereby "masking" the explicit $\mathcal{C}$-symmetry breaking due to the flux. However, when the SSH model is driven out of equilibrium by a quench, the $\mathcal{S}$-symmetry is dynamically broken [24,25]. This is because, despite its similarity with the unitary charge-conjugation $\mathcal{C}_0$ [see Eq. (9)], $\mathcal{S}$ is antiunitary. Physically, this means that the tsunami effect, i.e., the extensively long lasting rigidity to the nonlocal $\mathcal{C}$ breaking caused by a magnetic flux, is by no means due to the chiral symmetry protection, which only occurs "accidentally" in the equilibrium ground state.

In order to support this conclusion, one can introduce a local quantifier $Q_{\rm loc}^\nu$ of symmetry breaking, which measures at any time "how much" the symmetry ($\nu = \mathcal{C}, \mathcal{S}$) is broken at local level in the instantaneous quantum state. While details about the definition and the evaluation of these quantifiers will be given thoroughly in the next section and in Appendix D, we feel appropriate to anticipate here the dynamical behavior of these local quantifiers $Q_{\rm loc}^\nu$, illustrated in Fig. 4(d). Specifically, the green curve depicts the local quantifier of the chiral symmetry breaking, which becomes non vanishing immediately after the quench, as a hallmark of the dynamical symmetry breaking of $\mathcal{S}$. In contrast, the red curve describes the quantifier for the charge conjugation symmetry $\mathcal{C}$, which remains exponentially small (in system size) until the time τ_1^*, i.e., the time at which correlations start to experience the presence of the flux. Only for $\tau > \tau_1^*$, the SSH model can feel the actual breaking of the $\mathcal{C}$ symmetry. In turn, this also shows that, despite the abrupt dynamical breaking of the chiral symmetry, local observables may still be rigid to dynamical changes.

V. SYMMETRY BREAKING QUANTIFIERS

In this section, we introduce and discuss in details the quantifiers of symmetry breaking that have been anticipated at the end of the previous section. These quantities are meant to identify "how much" a given symmetry is broken in a quantum state. This will enable us to quantitatively distinguish the impact of local versus nonlocal $\mathcal{C}$-symmetry breaking and also to characterize the difference between breaking the discrete symmetries relevant for our problem, namely charge conjugation symmetry $\mathcal{C}$ and chiral symmetry $\mathcal{S}$. Similar ideas, based on entanglement, have been recently applied in Ref. [41] to quantify the breaking of continuous symmetries.

A. General definition of $\mathcal{C}$-symmetry and $\mathcal{S}$-symmetry breaking quantifiers

1. *Charge conjugation*

We start from the charge conjugation symmetry. As discussed in Sec. II, if a quantum many-particle state $\boldsymbol{\rho}$ is $\mathcal{C}$-symmetric ($\mathcal{C}_\theta\boldsymbol{\rho}\mathcal{C}_\theta^\dagger = \boldsymbol{\rho}$), then the related single-particle reduced density matrix ρ fulfills Eq. (4). If the quantum state $\boldsymbol{\rho}$ breaks $\mathcal{C}$ symmetry, i.e., if $\mathcal{C}_\theta\boldsymbol{\rho}\mathcal{C}_\theta^\dagger \neq \boldsymbol{\rho}$ for any set of phases $\{\theta\}$, Eq. (4) is also violated [42], and one can introduce a quantifier for $\mathcal{C}$-symmetry breaking of the quantum state in terms of the single-particle density matrix. We shall consider two different quantifiers.

Global quantifier. The first natural option, straightforwardly suggested by Eq. (4), is to define

$$\begin{aligned} Q_{\rm glob}^{\mathcal{C}} &= \frac{1}{\sqrt{2L}} \min_{\{\theta\}} ||b^{\mathcal{C}}(\{\theta\})|| \\ &= \frac{1}{\sqrt{2L}} \min_{\{\theta\}} \sqrt{\sum_{i,j=1}^{L} \sum_{\alpha,\beta=A,B} |b^{\mathcal{C}}_{j\alpha,i\beta}(\{\theta\})|^2}, \end{aligned} \tag{40}$$

where

$$b^{\mathcal{C}}(\{\theta\}) = \rho + \mathsf{U}_\theta^*\rho^*\,\mathsf{U}_\theta - \mathbb{I} \tag{41}$$

is a Hermitean matrix in the single-particle Hilbert space, $||b^{\mathcal{C}}|| = \sqrt{(b^{\mathcal{C}})^\dagger b^{\mathcal{C}}}$ is its norm, and the minimum is computed over all possible realizations of phases in Eq. (2). Since U_θ is diagonal in real space, the matrix $\mathsf{U}_\theta^*\,\rho^*\,\mathsf{U}_\theta$ appearing in Eq. (4) differs from ρ^* simply by additional phases in the off-diagonal entries. Moreover, by noticing that $\rho + \mathsf{U}_\theta^*\rho^*\,\mathsf{U}_\theta$ is a positively defined matrix, it can be shown that $Q_{\rm glob}^{\mathcal{C}}$ represents the minimal mean squared deviation of its eigenvalues $\lambda^{(s)}(\{\theta\}) \geqslant 0$ (with $s = 1, , \ldots, 2L$) from the $\mathcal{C}$-symmetric case $\lambda^{(s)}(\{\theta\}) \equiv 1$, i.e.,

$$Q_{\rm glob}^{\mathcal{C}} = \min_{\{\theta\}} \sqrt{\frac{1}{2L}\sum_{s=1}^{2L} (1 - \lambda^{(s)}(\{\theta\}))^2}. \tag{42}$$

We shall dub such a quantifier *global*, for it involves the *entire* single-particle density matrix ρ, which can therefore by used to compute expectation values of any (local or nonlocal) one-body observables.

Local quantifier. If, however, one is interested in measuring observables localized in one specific portion of the lattice, the knowledge of the entire ρ is unnecessary, and only a sub-block of ρ is needed. For definiteness, let us focus, e.g., on one lattice site $P^* = (j^*, \alpha^*)$. In order to evaluate, the expectation values of the local density $\langle c^\dagger_{P^*} c_{P^*}\rangle$ at P^*, of the intercell or intracell currents $\langle \hat{J}^{\text{intra}}_{j^*}\rangle$ and $\langle \hat{J}^{\text{inter}}_{j^*}\rangle$ across P^* [see Eq. (32) or (33)], or also to compute the correlation $\langle c^\dagger_{P^*} c_P\rangle$ between P^* and any other lattice site $P = (j^* + l, \beta)$, only the (j^*, α^*)-th row (or column) of ρ is used. In particular, if the system is translationally invariant, the expectation value of a local observable is actually independent of the cell, and correlations only depend on the spatial cell distance, implying that the choice of the reference cell j^* is irrelevant. One can thus introduce a *local* $\mathcal{C}$-breaking quantifier as

$$\begin{aligned} Q^{\mathcal{C}}_{\text{loc}} &= \min_{\{\theta\}} \left| b^{\mathcal{C}}_{j^*\alpha^*}(\{\theta\}) \right| \\ &= \min_{\{\theta\}} \sqrt{\sum_{i=1}^{L} \sum_{\beta=A,B} \left| b^{\mathcal{C}}_{j^*\alpha^*,i\beta}(\{\theta\}) \right|^2}. \end{aligned} \tag{43}$$

A few remarks are in order. First, we note that both quantifiers (40) and (43) are defined upon minimization over all possible choices of the $\{\theta\}$ phases appearing in the definition of charge conjugation Eqs. (1) and (2). Because each phase set $\{\theta\}$ identifies a gauge transformation [see Eqs. (10) and (11)], the minimizing phase set $\{\theta\}$ also corresponds to the optimal gauge $[g]$, where the $\mathcal{C}_0$ symmetry is broken the least. This minimization is needed since $\mathcal{C}$ symmetry may be present, but hidden in a unsuitable choice of the gauge, like, e.g., in the case where model (14) is defined in OBCs.

Second, because expectation values of observables must be gauge independent, they must be evaluated by writing both the state and the operator in the same gauge, i.e.,

$$\langle \boldsymbol{O}\rangle = \text{tr}[O\rho] = \text{tr}[O(\{\theta\})\rho(\{\theta\})], \tag{44}$$

where $\boldsymbol{O} = \sum_{I,J} O_{IJ} c^\dagger_I c_J = \sum_{I,J} (O(\{\theta\})_{IJ} \tilde{c}^\dagger_I \tilde{c}_J$ is a one-body observable, and I and J is a compact notation for the site, $I = (i, \alpha)$ and $J = (j, \beta)$.

2. Chiral transformation

Proceeding similarly for the chiral transformation Eq. (39), one can prove (see Appendix A for details) that, if $\boldsymbol{\rho}$ is symmetric under the chiral transformation ($\mathcal{S}\boldsymbol{\rho}\mathcal{S}^\dagger = \boldsymbol{\rho}$), then the single-particle density matrix ρ fulfills

$$(\rho - \mathbb{I}/2) + \mathsf{U}_0 (\rho - \mathbb{I}/2) \mathsf{U}_0 = 0, \tag{45}$$

where U_0 is given by Eq. (7). Note that, differently from Eq. (4), the second term of Eq. (45) does not contain ρ^*. Introducing the matrix

$$b^S = \rho + \mathsf{U}_0 \rho \mathsf{U}_0 - \mathbb{I}, \tag{46}$$

the global and local quantifiers of chiral symmetry breaking are defined as

$$Q^S_{\text{glob}} = \frac{1}{\sqrt{2L}} ||b^S|| = \frac{1}{\sqrt{2L}} \sqrt{\sum_{i,j=1}^{L} \sum_{\alpha,\beta=A,B} \left| b^S_{j\alpha,i\beta} \right|^2} \tag{47}$$

and

$$Q^S_{\text{loc}} = \left| b^S_{j^*\alpha} \right| = \sqrt{\sum_{i=1}^{L} \sum_{\beta=A,B} \left| b^S_{j^*\alpha,i\beta} \right|^2}. \tag{48}$$

Notice that no minimization over the phase sets $\{\theta\}$ is needed for the quantifiers Q^S_{glob} and Q^S_{loc} because the chiral transformation Eq. (38) is unaffected by gauge transformations (10), due to its antilinear character.

B. Quantifiers for the ground state of the two band model Eq. (14)

Let us now harness the quantifiers introduced above to evaluate the amount of symmetry breaking on the ground state of the two-band model (14). In particular, we shall compare the effects of a local $\mathcal{C}$ breaking ($U \neq 0$ and $\varphi = 0$) to the case of a nonlocal $\mathcal{C}$ breaking ($U = 0$ and $\varphi \neq m\pi$). To this purpose, we observe that because the phase φ appears divided by the number $2L$ of sites in the Hamiltonian (14), for $L \gg 1$ each $\mathcal{C}$-breaking hopping term is of order $O(\varphi/L)$. In order to make a correct comparison, we thus require to have the same scaling law for the local $\mathcal{C}$-symmetry breaking induced by the on-site potential, and we shall re-express U in Eq. (14) as

$$U = \frac{u}{L}. \tag{49}$$

In this way, the nondimerized case [$v = w$ in Eq. (14)] and the dimerized case [$v \neq w$] describe a metal and an SSH insulator in the thermodynamic limit, respectively, with a small additional $\mathcal{C}$-breaking term $O(\varphi/L)$ or $O(u/L)$.

We have first considered the global $\mathcal{C}$-symmetry breaking quantifier $Q^{\mathcal{C}}_{\text{glob}}$ in Eq. (40). The minimization over the phase set $\{\theta\}$, performed over various physically reasonable phase choices [43], leads to the result shown in Fig. 5(a), where the global quantifier $Q^{\mathcal{C}}_{\text{glob}}$ is plotted for all these cases as a function of the systems size L. All curves in the log-log plot exhibit a linear behavior, indicating that $Q^{\mathcal{C}}_{\text{glob}}$ is always decaying *algebraically* with the system size L, with a power law determined by the slope. In particular, $Q^{\mathcal{C}}_{\text{glob}} \sim 1/\sqrt{L}$ in the metallic case (red and black curves), while $Q^{\mathcal{C}}_{\text{glob}} \sim 1/L$ is found for the insulating SSH case (cyan and blue curves), regardless of whether the symmetry is broken locally by the staggered potential U or nonlocally by the flux φ.

Let us now turn to the local quantifier in Eq. (43). For definiteness, we have chosen $P^* = (L/2, A)$ as a reference site, i.e., the site $\alpha^* = A$ in the "central" cell $j^* = L/2$, and we have computed how $Q^{\mathcal{C}}_{\text{loc}}$ scales with L for the various cases, as displayed in Fig. 5(b). For a metallic ground state where the $\mathcal{C}$ symmetry is broken locally (red curve) and nonlocally (black curve), $Q^{\mathcal{C}}_{\text{loc}}$ still exhibits an algebraic decay $Q^{\mathcal{C}}_{\text{loc}} \sim 1/\sqrt{L}$ with the system size. Similarly, for the insulating SSH ground state an algebraic decay $Q^{\mathcal{C}}_{\text{loc}} \sim 1/L$ is again observed when the $\mathcal{C}$ symmetry is broken locally by the on-site staggered

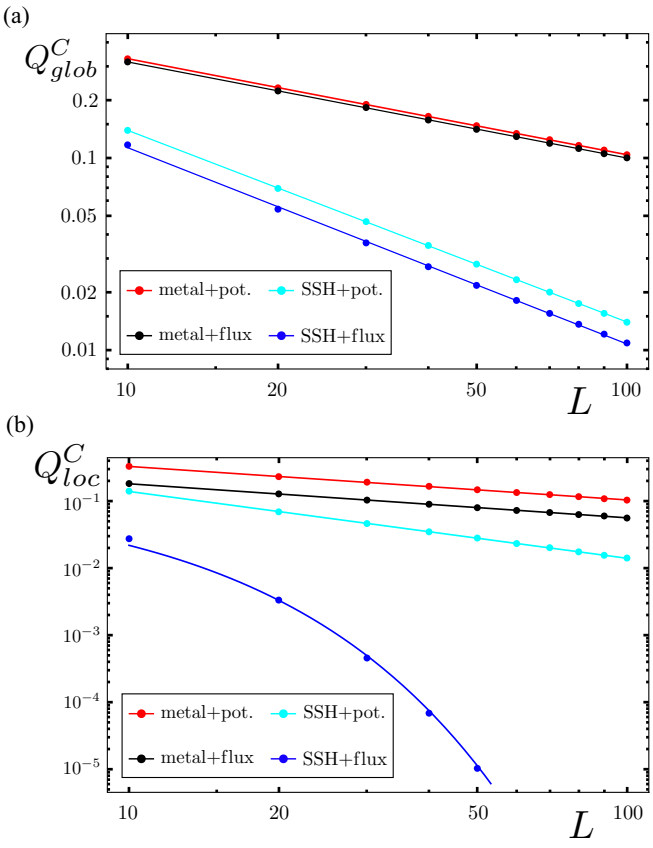

FIG. 5. (a) The global quantifier $Q^C_{\rm glob}$ of $\mathcal{C}$-symmetry breaking, Eq. (40), is shown in a log-log scale as a function of the number of cells L, for the ground states of four different Hamiltonians: the metallic case ($v = w$) and the insulating SSH case ($v = 1$ and $w = 0.7$), where the $\mathcal{C}$ symmetry is broken locally by an on-site potential $u = 1$ (red and cyan curves, respectively), and broken nonlocally by a flux $\varphi = \pi/2$ (black and blue curves, respectively). (b) The behavior of the local quantifier $Q^C_{\rm loc}$ of $\mathcal{C}$-symmetry breaking, Eq. (43), is shown in a log-log scale as a function of L, for the same ground states as in panel (a). For the case of the SSH insulator with $\mathcal{C}$ symmetry broken nonlocally by the flux (blue curve), $Q^C_{\rm loc} \sim \exp[-L/\Lambda]$ decreases exponentially with the system size L (here $\Lambda \simeq 5.3$), in striking contrast with the algebraic decay of the other local quantifiers and of all global quantifiers.

potential (cyan curve). Thus, in all these three cases, the local quantifier $Q^C_{\rm loc}$ in Fig. 5(b) exhibits the same scaling behavior as the corresponding global quantifier $Q^C_{\rm glob}$ shown in Fig. 5(a). However, in the case of an insulating SSH ground state where the $\mathcal{C}$ symmetry is broken nonlocally by the flux, one finds an *exponential* decay for the local quantifier $Q^C_{\rm loc} \sim \exp(-L/\Lambda)$ with Λ depending on the dimerization parameter r, as shown by the blue curve in Fig. 5(b).

The strikingly different scaling law of $Q^C_{\rm loc}$ obtained in the case of SSH model with flux, as compared to both $Q^C_{\rm loc}$ in the other cases and to the global quantifier $Q^C_{\rm glob}$ in all cases, provides a quantitative characterization of the insulator local rigidity to the flux from the perspective of charge conjugation symmetry breaking.

At a mathematical level, this difference originates from the different phase sets $\{\theta\}$ that minimize the quantifiers Eqs. (40) and (43) in the various cases. While these technical aspects are discussed in details in Appendix D, here we point that the local insensitivity of insulators to a nonlocal symmetry breaking induced by the flux can be understood in more physical terms as follows. Because expectation values $\langle \boldsymbol{O} \rangle$ are independent of the gauge choice, when considering observables $\boldsymbol{O}_{P^*}$ localized around (say) an arbitrarily chosen site $P^* = (j^*, \alpha^*)$, it is always possible to evaluate $\langle \boldsymbol{O}_{P^*} \rangle$ in the gauge sketched in Fig. 3(b), where the flux is accumulated along a link located farther than the localization length λ from P^*. This is realized by inserting in Eq. (10) the phase set $\{\theta_\ell\}$ given in Eq. (20). In such a gauge, the (j^*, α^*)th row of the single-particle density matrix $\rho(\{\theta_\ell\})$, which contains the actual entries involved in the evaluation of $\langle \boldsymbol{O}_{P^*} \rangle$ through Eq. (44), becomes effectively independent of the flux phase φ, due to the finite localization length of the insulator [see Fig. 8(b) in Appendix D]. At the same time, any possible spur of φ also disappears from the expression $O_{P^*}(\{\theta_\ell\})$ of the local operator in that gauge, precisely because it is localized around P^* only. This is the case for the on-site density operator, but also, e.g., for the current operator across P^*, where the flux phase appearing in the native gauge [see Eqs. (32) in (32)] is removed by the gauge transformation from the neighborhood of P^*. In conclusion $\langle \boldsymbol{O}_{P^*} \rangle$ is independent of the flux.

C. Dynamical evolution of the quantifiers

There is one further interesting advantage provided by the introduced symmetry breaking quantifiers $Q_{\rm glob}$ and $Q_{\rm loc}$. Because they are functions of the single-particle density matrix ρ of the system, as ρ dynamically evolves, one can monitor how the amount of symmetry breaking changes with time when the system is driven out of equilibrium. To this purpose, some care must be taken for the charge conjugation quantifiers, though. Indeed, if the minimization over the phase set $\{\theta\}$ in Eqs. (43) and (48) were performed at every time, the minimizing set $\{\theta\}(t)$ would change the definition of charge conjugation transformation $\mathcal{C}_{\theta(t)}$ on the run [see Eqs. (1) and (2)]. This would have serious implications, for it would lead to a time-dependent gauge transformation [see Eq. (11)] and thereby introduce a vector potential in the Hamiltonian (14) describing a spurious space and time-dependent electric field, with vanishing circulation along the ring. In order to avoid such an unphysical effect, one has thus to first determine the phase set $\{\theta\}^i$ minimizing $Q^C_{\rm glob}$ and $Q^C_{\rm loc}$ for the density matrix of the initial state. This identifies the definition of charge conjugation transformation $\mathcal{C}_{\theta^i}$ that is the least broken at $t = 0$. Then, by keeping such phase set frozen, i.e., by consistently retaining the definition of $\mathcal{C}_{\theta^i}$, one can inserting the dynamically evolving $\rho(t)$ into $b^C(\{\theta^i\})$ in Eq. (41), and thus evaluate how $|b^C_{j^*\alpha^*}(\{\theta^i\})|$ changes with time. This is how we determined the red curve in Fig. 4(d), which shows that the $\mathcal{C}$ symmetry remains effectively unbroken until the time τ_1^*, causing the tsunami effect. In contrast, the chiral symmetry breaking quantifier $Q^S_{\rm loc}$ does not require any minimization over $\{\theta\}$ by definition, as observed in Sec. V A. The dynamical evolution is thus straightforwardly obtained by inserting $\rho(t)$ into Eqs. (46) and (48). The obtained green curve in Fig. 4(d) clearly shows that in a quenched SSH insulator threaded by a flux the chiral symmetry is dynamically broken immediately

after the quench, whereas this is not the case for the charge conjugation, which remains effectively unbroken up to the extensively long time τ_1^*, i.e., $t = L\hbar/4\gamma \mathrm{v}_m$.

We conclude by observing that, because the symmetry breaking quantifiers are based on the single-particle reduced density matrix ρ of the quantum state, they are closely related to measurable quantities. Indeed the diagonal entries of ρ describe the local particle density and can be directly measured, while its off-diagonal entries encode all two-point correlation functions, which can be experimentally detected with various techniques, e.g. quantum gas microscopy [44,45] and matter wave interferometry [46]. The symmetry breaking quantifier sets an upper bound for the deviations of density or correlation functions from the symmetric case. This is shown precisely in Fig. 4: As long as the $\mathcal{C}$-breaking quantifier remains negligible [red curve in panel (d)], the correlations and the density deviation do not feel the effect of the $\mathcal{C}$-breaking flux [see panels (a) and (b)]. Only after the quantifier has become a significant fraction of unity, can these quantities start to deviate from the zero-flux case.

VI. ROBUSTNESS OF THE EFFECT

While in Sec. IV the tsunami effect has been explicitly demonstrated in a clean and noninteracting system, we shall now relax these hypotheses and address the generality and robustness of this effect by studying its stability against disorder and interactions.

A. Effects of disorder

Let us start by introducing some disorder in the tunneling amplitudes of Eq. (14). We shall thus consider the disordered SSH Hamiltonian

$$H_{\mathrm{SSH}}^{\mathrm{dis}} = \gamma \sum_{j=1}^{L} \left(v_j \, e^{i\frac{\varphi}{2L}} c_{jA}^\dagger c_{jB} + w_j \, e^{i\frac{\varphi}{2L}} c_{jB}^\dagger c_{j+1A} + \mathrm{H.c.} \right) \tag{50}$$

with

$$\begin{aligned} v_j &= v(1+\sigma\,\xi_j), \\ w_j &= w(1+\sigma\,\eta_j). \end{aligned} \tag{51}$$

Here v and w represent the average magnitude of the tunneling amplitudes, σ is a parameter identifying the disorder strength, and $(\xi_j, \eta_j) \in [-1/2; 1/2]$, with $j = 1, \ldots, L$, are $2L$ uniformly distributed random numbers. Notice that disorder in the tunneling does not alter the $\mathcal{C}$-symmetry properties with respect to the clean case, and the Hamiltonian (50) exhibits charge conjugation symmetry for $\varphi = \pi m$ with $m \in \mathbb{Z}$.

We perform a quench in the average values v and w of Eq. (51) according to the protocol (24) and analyze the dynamics of the local density. Due to the lack of translational invariance, one has $n_{j,A/B} = 1/2 \pm \delta n_j$, where the local deviation δn_j from half filling now depends on the cell, in general. In Fig. 6, we report the dynamical behavior of δn on a given A site, which is qualitatively well representative of the result for any site, and also of the spatial average over all A sites (not shown here). While the green curve refers to the clean case ($\sigma = 0$) and is plotted as a reference, the orange and purple curves describe the effects of disorder strength $\sigma = 0.1$ and 0.2, respectively. As one can see, while the disorder strength reduces the amplitude of the tsunami effect, the qualitative behavior and the extensively long time needed for its appearance remain unaffected.

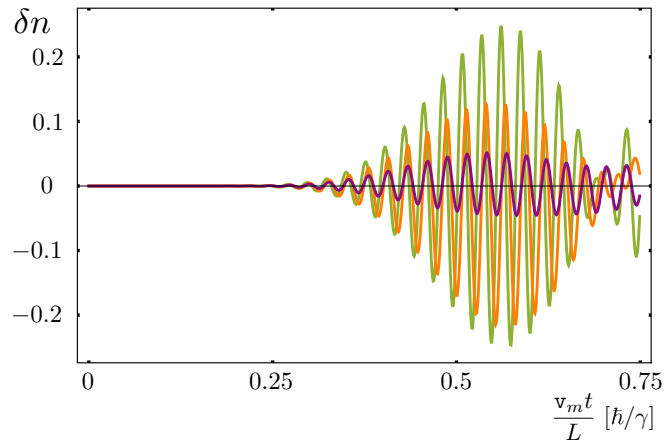

FIG. 6. Effects of disorder (51). The dynamical behavior of δn, the local density deviation from 1/2, is plotted as a function of time for a quenched SSH ring, for various values of the disorder strength σ [see Eq. (51)], namely, $\sigma = 0$ (clean case, green curve), $\sigma = 0.1$ (orange curve), and $\sigma = 0.2$ (purple curve). The number of cells is $L = 12$ (= 24 sites), the dimerization is $r = 0.1$, the flux phase is $\varphi = \pi/2$ and quench protocol is specified in Eq. (24).

In order to understand this effect, we recall that any finite amount of disorder in the tunneling amplitudes of a 1D system is sufficient to localize the single-particle eigenstates of the Hamiltonian in the thermodynamic limit [47,48]. However, in the case of a finite system, the localized versus extended nature of the single-particle eigenstates effectively depends on the ratio between localization length and system size. In particular, since the localization length depends on the single-particle energy, a fraction of the single-particle eigenfunctions might extend over the entire system for sufficiently weak disorder. Hence, the system behaves as if a fraction of the particles could still propagate throughout the ring and reveal the existence of the flux once the extensive time has elapsed.

B. Effects of interaction

Let us now probe the stability of the tsunami effect against particle-particle interaction. In particular, we shall add to the SSH Hamiltonian [Eq. (14) with $U = 0$] the following term:

$$H^{\mathrm{int}} = \gamma\, V \sum_{j=1}^{L} (n_{jA} + n_{j+1A} - 1)\left(n_{jB} - \frac{1}{2}\right) \tag{52}$$

describing a nearest neighbor interaction between particle density fluctuations $(n_{j\alpha} - 1/2)$ from the half filling value 1/2. Here V is the dimensionless coupling constant expressing the interaction strength in units of the energy unit γ appearing in Eq. (14). Importantly, the interaction term fulfills $\mathcal{S} H^{\mathrm{int}} \mathcal{S}^\dagger = H^{\mathrm{int}}$ (chiral symmetry) and $\mathcal{C}_\theta H^{\mathrm{int}} \mathcal{C}_\theta^\dagger = H^{\mathrm{int}}$ (charge conjugation symmetry) for any choice of θ phases in

Eqs. (1) and (2), so that the total Hamiltonian

$$H = \gamma \sum_{j=1}^{L} \left(v\, e^{i\frac{\varphi}{2L}} c^{\dagger}_{jA} c_{jB} + w\, e^{i\frac{\varphi}{2L}} c^{\dagger}_{jB} c_{j+1A} + \text{H.c.} \right) + H^{\text{int}} \tag{53}$$

still fulfills the chiral symmetry, while the charge conjugation symmetry is only broken by the global constraint imposed by a finite flux in the noninteracting SSH term.

For sufficiently strong interaction strength V, exceeding a critical value V_c, the half-filled ground state of the model (53) is known to exhibit a transition from a band insulator to an interaction-induced insulating phase. In particular, a repulsive interaction $V > V_c > 0$ leads to degenerate charge-density wave phases characterized by a uniform density imbalance between A and B sublattices. By contrast, an attractive interaction $V < -V_c < 0$ leads to a regime of degenerate states characterized by phase separation, where fermions equally populate the A and B sublattices while remaining compressed in one half of the system [49]. The critical value V_c of the transition depends on the dimerization strength and on the sign of interaction, e.g., for $r = 1/3$ one has $V_c = 4$ for the repulsive case, while $V_c \simeq 0.87$ for the attractive case [49].

While the analysis of the dynamical effects of strong interaction is far beyond the purposes of the present work, one can argue that, because the ground state on the noninteracting model is insulating, the inclusion of sufficiently weak interactions ($|V| \ll V_c$), leads to an interacting ground state that is nondegenerate and adiabatically connected to the noninteracting case. Moreover, when the quench is applied, the velocity of the resulting excitations is expected to be sightly enhanced by a repulsive interaction and slightly reduced by an attractive one [50,51]. Because such velocity determines the spreading of correlations and thereby the onset of the tsunami effect, we expect interactions to modify quantitatively, but not qualitatively, the phenomenon. In order to test these expectations, we have adopted a numerically exact diagonalization method to determine the initial interacting ground state and to investigate the out-of-equilibrium behavior governed by the Hamiltonian (53), under the quench protocol (24). While being limited to small system sizes (here $L = 7$, i.e., 14 sites), this approach allows us to explore the dynamical evolution at arbitrary long times.

The result is shown in Fig. 7, which displays the dynamical evolution of the density deviation δn for a quenched interacting SSH model with dimerization $r = 0.1$, threaded by a flux $\varphi = \pi/2$, and for three values of interaction V. The green curve refers to the noninteracting case ($V = 0$) and is meant as a reference case, while the red and black curves describe the cases of weakly repulsive ($V = 0.1$) and weakly attractive interaction ($V = -0.1$), respectively. As one can see, the density deviation δn still remains extremely small for an extensively long time, after which it starts to take seizable values, therefore indicating that the tsunami effect is not destroyed by weak interactions. Also, an inspection of the density oscillation maxima shows that in the repulsive (attractive) case the onset of the tsunami effect occurs slightly earlier (later) than the non interacting case, in agreement with our expectations. We note, however, that attractive interactions tend to suppress the magnitude of the fluctuations more than the repulsive case. This seems to be the dynamical counterpart of what happens for the ground state, where, for given dimerization r and interaction magnitude $|V|$ of interaction, the attractive case is closer to the critical value V_c than the repulsive case.

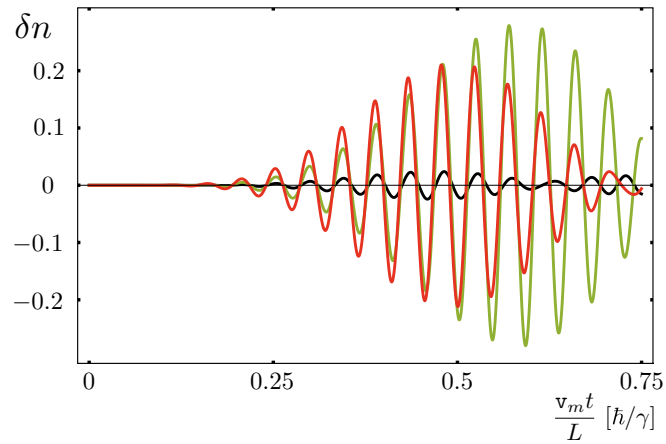

FIG. 7. Effects of interaction term Eq. (52). The dynamical behavior of the local density deviation δn is plotted as a function of time for a SSH ring with $L = 7$ cells (= 14 sites), threaded by a flux ($\varphi = \pi/2$) and undergoing a quench (24) with dimerization $r = 0.1$, for various values of the interaction strength V, namely, $V = 0$, (green curve), $V = +0.1$ (red curve), and $V = -0.1$ (black curve).

VII. DISCUSSION AND CONCLUSIONS

We have investigated the quantum dynamics of a quenched fermionic system on a 1D dimerized ring-shaped lattice with PBCs. By analyzing the effects of an explicit breaking of the charge-conjugation symmetry $\mathcal{C}$ on the local observables and correlations, we have shown that the impact of the symmetry breaking in the Hamiltonian is felt by local observables in a way that heavily depends on the localization properties of the initial quantum state and on the local *vs* nonlocal nature of the $\mathcal{C}$ breaking. In particular, if the $\mathcal{C}$ symmetry is broken nonlocally by a magnetic flux and the localization length of the quantum state is finite (insulator), local observables behave is if $\mathcal{C}$ symmetry were unbroken, in striking contrast with what happens in metals or in insulators with $\mathcal{C}$ symmetry broken locally by an on-site potential.

While at equilibrium or in adiabatically slow dynamics, the rigidity of an insulator to a flux was known, the most spectacular effect that we found is that such rigidity to the $\mathcal{C}$-symmetry breaking persists even in far from equilibrium conditions, i.e., when a quantum quench is applied. In particular, local observables effectively retain their $\mathcal{C}$-symmetric values for a time that scales linearly with the system size, and only after such time can the effects of nonlocal $\mathcal{C}$-symmetry breaking become visible. A clear evidence of this phenomenon, that we have dubbed tsunami effect, is shown in Fig. 1, which displays the dynamical evolution of the local particle density deviation δn from $1/2$ resulting from a quench, and reveals the striking difference between local $\mathcal{C}$-symmetry breaking (RM

model with on-site potential) and nonlocal $\mathcal{C}$-symmetry breaking (SSH model with flux). In the strongly dimerized limit, we have also been able to determine an analytical expression for the dynamical behavior of δn [see Eq. (27) and Fig. 2], characterized by an exponential suppression as a function of the system size L before the tsunami onset [see Eq. (28)]. As discussed in Sec.IV B, the tsunami effect is not limited to the quench protocol (24) and to the strongly dimerized limit. It is a general phenomenon occurring for any quench protocol, provided that the $\mathcal{C}$ symmetry is broken by a flux and the initial state is insulating. In contrast, when the initial state is metallic, the deviation δn appears as $O(1/L)$ right after the quench [see Eq. (31)].

The long time invisibility of the $\mathcal{C}$-breaking flux at local level is a physical effect that is of course completely independent of the gauge chosen for the vector potential. However, in each arbitrary point where, e.g., the density is evaluated, it can most suitably understood in the gauge sketched in Fig. 3(b), where the entire flux phase is accumulated to opposite side of the ring.

Moreover, the tsunami effect also manifests itself in the correlation function, as displayed in Fig. 4(a). In fact, the earliest manifestation of the flux occurs in the nonlocal correlations of two maximally separated points ($l = \pm L/2$), again only after an extensive time τ_1^* in Eq. (37). As shown in Fig. 4(c), this time can also be seen as the moment when the Wannier function localization length λ, which is spreading as a result of the quench, reaches its maximal value and has thus explored to entire ring, thereby experiencing the presence of the nonlocal flux. As highlighted by red and black vertical dashed lines in Fig. 4, the time τ_2^* where the tsunami effect is perceived on the density, i.e., on local correlations at $l = 0$, is twice longer than τ_1^*.

In order to characterize this phenomenon, we have also introduced the quantities $Q_{\rm glob}$ and $Q_{\rm loc}$, which quantify how strongly a symmetry is broken in an arbitrary quantum state by means of its single-particle density matrix, at global and at local level, respectively. This has enabled us to obtain two results. First, as far as the equilibrium ground state is concerned, the known insensitivity of insulator to a flux can be interpreted as a local rigidity to the $\mathcal{C}$-symmetry breaking. Explicitly, the "amount" $Q^{\mathcal{C}}_{\rm loc}$ of local $\mathcal{C}$-symmetry breaking of a SSH ring threaded by a flux is found to be exponentially small in the system size L, while it only exhibits an algebraic decay in insulators with local $\mathcal{C}$-symmetry breaking and in metals (see Fig. 5). We have also shown that this can be straightforwardly understood in a suitable gauge, as illustrated in Fig. 3(b). Second, in terms of out of equilibrium dynamics, the obtained evolution of the local quantifiers $Q^{\mathcal{C}}_{\rm loc}$ and $Q^{\mathcal{S}}_{\rm loc}$ has allowed us to demonstrate that the tsunami effect, i.e., the predicted robustness to charge conjugation symmetry breaking, is completely unrelated to the presence of the chiral symmetry, which is instead lost right after the quench because of its dynamical breaking, as shown in Fig. 4(d). Furthermore, by including weak disorder and density-density interaction, we have proven that the tsunami effect is not destroyed by these effects (see Figs. 6 and 7).

Space-time scaling regime. We also emphasize that our work represents further advances in the exploration of the space-time scaling regime, where the out of equilibrium quantum dynamics is analyzed for timescales t that are proportional to the system size L. It was recently shown that this regime offers a different perspective to identify out of equilibrium topological classification of quantum systems [28], as compared to the more conventional short time limit [12] and adiabatic limit [52–56]. In terms of the parameter $\eta = 2\pi t/L$ that identifies the ratio between time and system size (see Ref. [28]), the standard thermodynamic limit corresponds to $\eta \to 0$. In this limit, the system cannot experience the presence of the flux and it behaves as if charge conjugation were effectively unbroken. In contrast, at finite values of η, non trivial effects emerge. Specifically, by re-expressing our result Eq. (27) in terms of η, the tsunami effect can be regarded to as a *dynamical crossover* characterizing the density deviation δn. Indeed, for $\eta < \eta_c$, where $\eta_c = \pi\hbar/\gamma \mathsf{v}_m$, we find an exponential suppression $\delta n \sim e^{-\kappa(\eta)L}$ as a function of the system size, typical of an insulator [with $\kappa(\eta \to \eta_c) = 0$]. In contrast, for $\eta > \eta_c$, one finds the slow algebraic decay $\delta n \sim 1/\sqrt{L\eta^3}$ with L, typical of a metal, so that the quantum nonlocality induced by a flux appears. Our result thus proves that only in the space-time scaling regime one can observe such "insulator-to-metal" dynamical crossover.

Experimental realizations. Finally, we would like to discuss some possible strategies to implement the model in Eq. (14) and to probe its out-of-equilibrium behavior. Although dimerized lattice models have been realized with cold atoms in optical lattices in various setups over the last decade [57–61], most of these implementations are based on lattices with OBCs, whereas a crucial aspect for the observation of the tsunami effect is a ring-shaped geometry with PBCs and a flux. Recent experimental advances offer promising perspective to realize this type of setup. A first proposal is based on Rydberg atoms in optical tweezers [62], which allow one to engineer spin models equivalent to the fermionic Hamiltonians discussed here, also with dimerization [63]. In particular, in recent experiments based on twezeer engineering, a tunable flux was obtained by exploiting the synthetic dimension of Rydberg atoms [64,65], and ring-shaped geometries have also been recently designed [66]. A further experimental platform suitable to test our findings could possibly be based on SU(N) ultracold fermions in optical lattice [67–69]. In that case, effective rings can be created in synthetic dimension by coupling the different internal states of the specific atomic species. More precisely, the use of Raman lasers enables one to convert an internal state into a different one, thereby mimicking effective tunneling processes, with a twofold advantage. On one hand the couplings between different internal states are tunable, thus making possible to achieve effective dimerizations. On the other hand, complex tunneling processes can be easily engineered [9,10], in order to mimic the effect of a magnetic flux. Finally, quantum gas microscopy [44], widely used in tweezer and optical lattice setups, allows for an accurate detection of the local density and therefore for an accurate probing of the effects predicted here.

ACKNOWLEDGMENTS

F.D. acknowledges financial support from the Italian Centro Nazionale di Ricerca in High Performance Computing, Big Data and Quantum Computing, funded by European

Union - NextGenerationEU (Grant No. CN00000013) and the PRIN Project 2022B9P8LN, funded by the Italian Ministry of University and Research. J.C.B. acknowledges financial support from the German Research Foundation (DFG) through the Collaborative Research Centre SFB 1143 (Project No. 247310070), the Cluster of Excellence ct.qmat (Project No. 390858490), and the DFG Project 419241108.

APPENDIX A: PROOF OF THE THEOREM

In this Appendix, we prove the theorem stated in Sec. II A. Let us assume that the many-particle state $\boldsymbol{\rho}$ of the system is invariant under charge conjugation, i.e., $\mathcal{C}\boldsymbol{\rho}\mathcal{C}^\dagger = \boldsymbol{\rho}$. In order to prove Eq. (4), we introduce the multi-index $J = (j, \alpha)$ to label the cell j and the site $\alpha = A, B$, and observe that the charge conjugation transformation (1) can be written as

$$\mathcal{C} c_I^\dagger \mathcal{C}^\dagger = \sum_N \mathsf{U}_{IN} c_N, \tag{A1}$$

where U is the matrix written in Eq. (2). In the following proof, we shall actually be slightly more general, and derive the relation of the single-particle density matrix for an arbitrary unitary matrix U, whence Eq. (4) will follow as a particular case. We thus observe that the expectation value of any one-body observable $\boldsymbol{O} = \sum_{I,J} O_{IJ} c_I^\dagger c_J$ can be written as

$$\langle \boldsymbol{O} \rangle = \mathrm{Tr}\{\boldsymbol{\rho}\, \boldsymbol{O}\} = \sum_{I,J} O_{IJ} \mathrm{Tr}\{\boldsymbol{\rho}\, c_I^\dagger c_J\} = \mathrm{tr}\{O\rho\}, \tag{A2}$$

where ρ is the single-particle reduced density matrix and the symbols "Tr" and "tr" denote traces over the Fock space and the single-particle Hilbert space, respectively. At the same time, because of the $\mathcal{C}$ symmetry, the expectation value can also be written as (sum over the repeated indices is implicit here below)

$$\begin{aligned}
\langle \boldsymbol{O} \rangle &= \mathrm{Tr}\{\mathcal{C}^\dagger \boldsymbol{\rho}\, \mathcal{C} \boldsymbol{O}\} = O_{IJ} \mathrm{Tr}\{\boldsymbol{\rho}\, \mathcal{C} c_I^\dagger \mathcal{C}^\dagger \mathcal{C} c_J \mathcal{C}^\dagger\} \\
&= O_{IJ} \mathsf{U}_{IN} \mathsf{U}^*_{JM} \mathrm{Tr}\{\boldsymbol{\rho}\, c_N c_M^\dagger\} \\
&= O_{IJ} \mathsf{U}_{IN} \mathsf{U}^*_{JM} \mathrm{Tr}\{\boldsymbol{\rho}(\,\delta_{NM} - c_M^\dagger c_N)\} \\
&= O_{IJ} \mathsf{U}_{IN} \mathsf{U}^*_{JM} (\delta_{NM} - \rho_{NM}) \\
&= O_{IJ}(\delta_{IJ} - [\mathsf{U}\rho\,\mathsf{U}^\dagger]_{IJ}) = O_{IJ}(\delta_{IJ} - [\mathsf{U}\rho\,\mathsf{U}^\dagger]^*_{JI}) \\
&= \mathrm{tr}\{O[\mathbb{I} - (\mathsf{U}\rho\,\mathsf{U}^\dagger)^*]\}.
\end{aligned} \tag{A3}$$

Because both equalities (A2) and (A3) must hold for any operator O, one deduces that

$$\rho = \mathbb{I} - (\mathsf{U}\rho\,\mathsf{U}^\dagger)^*. \tag{A4}$$

So far in this proof, U is an arbitrary unitary matrix. In particular, in the case Eq. (2) considered in the Main text, one straightforwardly obtains Eq. (4). Moreover, by recalling that the diagonal entries of the single-particle density matrix are the expectation values of the particle density, $\langle n_{j\alpha} \rangle = \rho_{j\alpha, j\alpha}$, and by taking the diagonal entries of Eq. (4), one deduces that $2\rho_{j\alpha,j\alpha} - 1 = 0\, \forall j, \alpha$, which straightforwardly implies Eq. (5). Finally, the statement (6) of the theorem was proven in Ref. [30].

In a similar manner, one can prove Eq. (45) related to the implication of chiral symmetry on the single-particle density matrix. The main difference with respect to the above proof is that, because of the antilinear character of $\mathcal{S}$, in the first line of Eq. (A3), one has to replace $O_{IJ} \to O^*_{IJ} = O_{JI}$. After substituting U with the matrix U_0 entering the definition (39) of chiral symmetry, Eq. (45) is eventually obtained.

APPENDIX B: CALCULATION OF THE DENSITY DEVIATION IN THE STRONGLY DIMERIZED LIMIT

Here we provide details about the calculation of the dynamical evolution of the site density resulting from the quench protocol (24) applied of the SSH model threaded by a flux φ. In particular, we shall demonstrate the asymptotic behavior Eq. (27). Exploiting the cell translational invariance one, can write

$$\begin{aligned}
n_\alpha(t) &\equiv \frac{1}{L}\sum_j \langle n_{j\alpha} \rangle = \frac{1}{L}\sum_k \langle n_{k\alpha} \rangle \\
&= \frac{1}{L}\sum_k (\rho_-)_{\alpha\alpha}(k,t) = \frac{1}{2} \pm \delta n(t),
\end{aligned} \tag{B1}$$

where the $\pm$ sign refers to $\alpha = A, B$, respectively. Recalling from Sec. IV B of the main text that the evolution of the k block is $\rho_-(k,t) = [\sigma_0 - \hat{\mathbf{d}}(k,t)\cdot\boldsymbol{\sigma}]/2$ and that $\hat{\mathbf{d}}(k,t)$ is given by Eq. (25), one has

$$\begin{aligned}
\delta n(t) &= \frac{1}{2L}\sum_k (\hat{\mathbf{d}}^i(k) \times \hat{\mathbf{d}}^f(k))_z \, \sin[2|\mathbf{d}^f(k)|\,\tau] \\
&= \frac{1-r^2}{2L}\sum_{k=-\pi}^{\pi} f\left(k + \frac{\varphi}{L}, \tau; r\right),
\end{aligned} \tag{B2}$$

where τ is the dimensionless time given in Eq. (26), r is the dimerization parameter, and

$$f(k,\tau;r) = \sin k \frac{\sin[2\tau\sqrt{1 + r^2 + 2r\cos k}]}{1 + r^2 + 2r\cos k}. \tag{B3}$$

Here we have exploited Eq. (16) and the form (24) of the quench protocol, where the pre and postquench Hamiltonian exhibit the same single-particle spectrum [see Eq. (17) for $U = 0$]. Because $f(k,\tau;r)$ is a 2π-periodic function of its argument k, by exploiting its Fourier series expansion $f(k,\tau;r) = (2\pi)^{-1}\sum_{n=-\infty}^{+\infty} c_n(\tau;r)\exp[ikn]$, some straightforward algebra enables one to rewrite

$$\delta n(t) = \frac{(1-r^2)}{4\pi}\sum_{m=-\infty}^{+\infty} c_{mL}(\tau;r) e^{im\varphi}, \tag{B4}$$

where

$$\begin{aligned}
c_{mL}(\tau;r) &= \int_{-\pi}^{\pi} dk\, f(k,\tau;r)\, e^{-ikmL} \\
&= \int_{-\pi}^{\pi} dk\, \sin k \frac{\sin[2\tau\sqrt{1 + r^2 + 2r\cos k}]}{1 + r^2 + 2r\cos k}\, e^{-ikmL}.
\end{aligned} \tag{B5}$$

By noting that $c_{-mL} = -c_{mL}$ and that $c_0 = 0$, one can rewrite Eq. (B4) as

$$\delta n(t) = i\frac{(1-r^2)}{2\pi}\sum_{m=1}^{+\infty} c_{mL}(\tau;r)\sin(m\varphi). \tag{B6}$$

So far, no approximation has been made. We shall now take the limit of strong dimerization $r \ll 1$ and approximate the coefficients (B5) as

$$c_{mL}(\tau; r) \simeq \int_{-\pi}^{\pi} dk \, \sin k \, \sin[2\tau(1 + r\cos k)] \, e^{-ik mL} = \frac{\pi mL}{2\tau r} \, i^{mL+1} J_{mL}(2\tau r)[e^{i2\tau} + (-1)^{mL} e^{-i2\tau}]. \quad \text{(B7)}$$

Assuming, e.g., L even and inserting Eq. (B7) into Eq. (B6), one obtains

$$\langle \delta \hat{n} \rangle \simeq -\sum_{m=1}^{+\infty} (-1)^{\frac{mL}{2}} \frac{mL}{2\tau r} J_{mL}(2\tau r) \cos(2\tau) \sin(\varphi m). \quad \text{(B8)}$$

In particular, in the time domain $2\tau r < 2L$, the first term with $m = 1$ is dominant over the other ones, and one finally obtains Eq. (27) that well captures the behavior of Fig. 2.

APPENDIX C: MAXIMALLY LOCALIZED WANNIER FUNCTIONS IN A FINITE SIZE RING

In this Appendix, we provide some details about the calculation of the MLWFs in a finite size ring-shaped lattice with cell translational invariance. The construction given below is based on the assumption to deal with a many-particle state that is the half-filled ground state of a two-band Hamiltonian, with a completely filled lower band and a completely empty upper band.

It is worth emphasizing that this approach is not limited to the initial ground state of the prequench Hamiltonian. Indeed, when a quench is performed in a system with cell translational invariance, the evolved many body state can always be regarded, at any given time t, as the half-filled ground state of a fictitious two-band Hamiltonian $H(t)$, where time appears as a parameter. This is because, as pointed out in Sec. IV B, the dynamical evolution of the single-particle density matrix is decoupled in k space, $\rho(t) = \oplus_{k\in BZ} \rho_-(k,t)$, where each evolved k block can be written as the ground state $\rho_-(k,t) = [\sigma_0 - \hat{\mathbf{d}}(k,t)\cdot\boldsymbol{\sigma}]/2$ of a two-level system with Hamiltonian $h(k,t) = \hat{\mathbf{d}}(k,t)\cdot\boldsymbol{\sigma}$, where $\hat{\mathbf{d}}(k,t)$ is the unit vector given in Eq. (25). Thus the evolved many-particle state at time t is the half-filled ground state of the fictitious Hamiltonian $H(t) = \gamma \sum_k c^\dagger(k)[\hat{\mathbf{d}}(k,t)\cdot\boldsymbol{\sigma}]c(k)$, with two flat bands $E_\pm(k) = \pm\gamma$.

Keeping in mind that the outline approach holds time by time, in the remaining part of this Appendix we shall make our notation lighter and drop the time t. We define the lower band Wannier state centered at the cell m, in the Bloch gauge g, as

$$|m-\rangle[g] = \frac{1}{\sqrt{L}} \sum_k e^{-ikm} \, e^{ig(k)} |k-\rangle, \quad \text{(C1)}$$

where, without any loss of generality, we have labeled the cells as $m = 0, \ldots, L-1$. Moreover, $|k-\rangle = |k\rangle \otimes |u_-(k)\rangle$ represents the single-particle lower band Bloch state in an arbitrary reference gauge, which we choose for definiteness as

$$|u_\pm(k)\rangle = [2(1 \mp \hat{d}_z(k))]^{-1/2} \begin{pmatrix} \hat{d}_x(k) - i\hat{d}_y(k) \\ \pm 1 - \hat{d}_z(k) \end{pmatrix}, \quad \text{(C2)}$$

where $\hat{d}_x(k)$, $\hat{d}_y(k)$, $\hat{d}_z(k)$ are the components of the unit vector $\hat{\mathbf{d}}(k)$ given in Eq. (25) and describing the quench dynamics of the two-band model (at time t).

The Wannier wave function is thus obtained by projecting the Wannier state (C1) on the real space state $\langle j\alpha|$, with $j = 0, , \ldots, L-1$ denoting any cell and $\alpha = A, B$ the sublattice index, and by exploiting $\langle j\,\alpha|k-\rangle = \exp[ikj]u_-^\alpha(k)/\sqrt{L}$. One obtains

$$\psi^g_{m,-}(j,\alpha) = \langle j\,\alpha|m-\rangle[g] = \frac{1}{L}\sum_k e^{ik(j-m)} \, e^{ig(k)} u_-^\alpha(k) \quad \text{(C3)}$$

and the corresponding probability of finding the particle in the jth cell is given by

$$P^g_{m-}(j) = \left|\psi^g_{m-}(j,A)\right|^2 + \left|\psi^g_{m-}(j,B)\right|^2. \quad \text{(C4)}$$

Note that, by construction, the various Wannier wave functions (C3) labeled by m are related to each other by a translation, namely $\psi^g_{m,-}(j,\alpha) = \psi^g_{0,-}(j-m,\alpha)$, so that it is sufficient to analyze the properties of the Wannier function $\psi_{0,-}$ labeled by the cell $m = 0$. For this reason, we shall henceforth drop the "$0,-$" subscript, and simply redenote $\psi_{0,-}(j,\alpha) \to \psi(j,\alpha)$ and $P_{0,-}(j) \to P(j)$.

In particular, we now want to evaluate the expectation value and the variance of the position operator. In an chain lattice with OBCs or in an infinitely long system the position operator is naturally defined as the Hermitean operator $\hat{X}$ whose one-body representation in the real space is identified by the diagonal matrix $X = \mathrm{diag}(1, \ldots, L-1, L) \otimes \sigma_0$, where L is the number of cells. However, because of the ring-shaped geometry considered here, such operator would manifestly break the PBCs. It is thus useful to adopt a regularized position operator $\hat{E} = \exp[i2\pi\hat{X}/L]$, which is not Hermitean, but whose one-body representation in the site basis is the diagonal matrix $E = \mathrm{diag}(e^{i\frac{2\pi}{L}}, e^{i\frac{4\pi}{L}} \ldots, 1) \otimes \sigma_0$ that fulfills the PBCs.

If one computes the expectation value of $\hat{E}$ on the single-particle Wannier function $\psi(j,\alpha)$, one obtains a complex number

$$\langle e^{i\frac{2\pi}{L}X}\rangle[g] \equiv \sum_j e^{i\frac{2\pi}{L}j} P^g(j) \equiv \Omega[g] \, e^{i\Theta[g]} \quad \text{(C5)}$$

with modulus $\Omega[g]$ and phase $\Theta[g]$. Equation (C5) can now be interpreted in terms of directional statistics [40], i.e., as the result of a stochastic process where points are randomly distributed on a unit circle according to the probability distribution $P^g(j)$, where $j = 0, , \ldots, L-1$ identifies an "angular" position $2\pi j/L$ along the circle, with the cell $L-1$ being the "left" nearest neighbor of cell 0. It is possible to show that the phase $\Theta[g]$ can be interpreted as the center of the Wannier function, which in the present case of a finite size system is gauge dependent, while the modulus $\Omega[g]$ in Eq. (C5) is closely related to the (gauge dependent) spread of the Wannier function through $\Delta X = \sqrt{1-\Omega^2}\, L/2\pi$. This correspondence becomes apparent when taking the thermodynamic limit, as we shall see below. However, even for a finite size system, one can notice that, if the distribution $P^g(j)$ is sharply peaked on one "angle" $2\pi j/L$, then the phase Θ in Eq. (C5) represents

such an angle and the modulus is maximal, $\Omega \simeq 1$. In contrast, if $P^g(j)$ is uniform along the ring, then the modulus Ω is minimal, $\Omega \simeq 0$.

In order to determine the MLWFs, we have to determine the gauge g^* such that $\Omega[g^*]$ is maximal, or equivalently $\Omega^2[g^*]$ is maximal. It is possible to find an exact solution to the problem. Indeed, we can rewrite Eq. (C5) as

$$\Omega[g]\, e^{i\Theta[g]} = \frac{1}{L^2}\sum_{j,\alpha}\sum_{k,q} e^{i(q+\delta k-k)j} e^{i[g(q)-g(k)]}(u^\alpha_-(k))^* u^\alpha_-(q)$$
$$= \frac{1}{L}\sum_k \langle u^g_-(k+\delta k)|u^g_-(k)\rangle, \tag{C6}$$

where we have denoted $|u^g_-(k)\rangle = e^{ig(k)}|u_-(k)\rangle$, $\delta k = 2\pi/L$, and we have exploited the Kronecker-δ obtained from the summation over j. The quantity $\xi^g_-(k) = \langle u^g_-(k+\delta k)|u^g_-(k)\rangle$ is a complex number whose modulus is gauge independent (and smaller than 1), while its phase critically depends on the gauge. In order to maximize $\Omega[g]$, one needs to choose the gauge g^*, in which the phases of all $\xi^g(k)$ in Eq. (C6) are as equal as possible, so that the terms sum as coherently as possible over k. Such optimal gauge choice can be determined by observing that

$$\varphi_{B-} = \sum_k \arg\{\xi^g_-(k)\} \qquad \mod 2\pi, \tag{C7}$$

which can be regarded as the discrete version of the Berry phase, is a gauge independent quantity. This becomes apparent by writing (mod2π)

$$\varphi_{B-} = \sum_k \mathrm{Im}(\ln \xi^g_-(k)) = \mathrm{Im}\left(\ln \prod_k \xi^g_-(k)\right)$$
$$= \mathrm{Im}\{\ln[, \ldots, \langle u^g_-(k+2\delta k)|u^g_-(k+\delta k)\rangle$$
$$\times \langle u^g_-(k+\delta k)|u^g_-(k)\rangle, \ldots,]\}$$
$$= \mathrm{Im}\left\{\ln\left[\mathrm{tr}\prod_k \rho_-(k)\right]\right\}, \tag{C8}$$

where $\rho_-(k) = |u^g_-(k)\rangle\langle u^g_-(k)|$ is a gauge invariant projector. Thus one can define the gauge $g^*(k)$ as

$$\arg\{\xi^{g^*}_-(k)\} = \mathrm{Im}\{\ln \xi^{g^*}_-(k)\} = \frac{\varphi_{B-}}{L} \quad \forall k, \tag{C9}$$

which represents the gauge, in which the (discrete version of the) Berry connection is constant. It is also possible to show that φ_{B-} tends to the actual Berry phase when taking the thermodynamic limit.

It is then straightforward to notice that such a gauge is characterized by the following properties. The phase Θ, which represents the angular center of the Wannier wavefunction, coincides with the discrete version of the Berry phase

$$\Theta[g^*] = \frac{1}{L}\varphi_{B-}, \tag{C10}$$

whereas the modulus Ω takes the maximal possible value

$$\Omega[g^*] = \max_{[g]} \Omega[g] = \frac{1}{L}\sum_k |\xi^{g^*}(k)| = \frac{1}{L}\sum_k |\xi^g(k)|. \tag{C11}$$

Furthermore, it is possible to show that, in the thermodynamic limit $L \to \infty$, i.e., $\delta k \to 0$, one has

$$\Theta[g] \to \Theta \equiv \left(\frac{2\pi}{L}\right)\frac{1}{2\pi}\int dk\, \langle u^g_-(k)|i\partial_k|u^g_-(k)\rangle, \tag{C12}$$

i.e., the Wannier center becomes gauge independent and, when converted into spatial coordinates $\langle X\rangle = L\Theta/2\pi$ (in units of the lattice spacing), it coincides with the known result reported in Refs. [37–39]. Moreover, the modulus Ω tends to

$$\Omega^2[g] \to \Omega^2 \equiv 1 - \left(\frac{2\pi}{L}\right)^2 \frac{1}{2\pi}\int dk\, ||\partial_k u^g_-(k)\rangle|^2$$
$$+ \left(\frac{2\pi}{L}\right)^2\left[\frac{1}{2\pi}\int dk\, \langle u^g_-(k)|i\partial_k|u^g_-(k)\rangle\right]^2, \tag{C13}$$

which implies that the Wannier spread in spatial coordinates reads

$$\Delta X = \sqrt{\langle X^2\rangle - \langle X\rangle^2} = \frac{L}{2\pi}\sqrt{1-\Omega^2} \tag{C14}$$

given in Ref. [36–39]. It is thus evident that maximizing Ω corresponds to minimizing the spreading of the Wannier functions.

In conclusion, it is possible to exactly find the MLWFs even in a finite size 1D ring-shaped lattice. Such functions have a center of mass with linear coordinate $\varphi_{B-}/2\pi$, where we have converted the angular position into the linear one through the factor $L/2\pi$. Moreover the angular spread of the MLWFs can be identified from Eq. (C14) as

$$\lambda = \frac{2\pi}{L}\Delta X = \sqrt{1-\Omega^2[g^*]}. \tag{C15}$$

This quantity is what we have plotted in Fig. 4(c)

APPENDIX D: MINIMIZATION OF SYMMETRY BREAKING QUANTIFIERS $\mathcal{Q}^{\mathcal{C}}_{\mathrm{glob}}$ and $\mathcal{Q}^{\mathcal{C}}_{\mathrm{loc}}$

Here we discuss some technical details about the phase set $\{\theta\}$ that minimizes the charge symmetry breaking quantifiers (40) and (43), in the various cases described in Fig. 5. It turns out that there are two types of sets minimizing the quantifiers $\mathcal{Q}^{\mathcal{C}}_{\mathrm{glob}}$ and $\mathcal{Q}^{\mathcal{C}}_{\mathrm{loc}}$. The first one is

$$\{\theta_u\} \equiv \begin{cases}\theta_{j,A} = +\delta/2 \\ \theta_{j,B} = -\delta/2\end{cases} \qquad j = 1, , \ldots, L \tag{D1}$$

with δ denoting a staggering, while the second one is given by Eq. (20).

When the flux is absent ($\varphi = 0$) and the $\mathcal{C}$ symmetry is broken locally by the on-site potential U, the staggering value minimizing the quantifiers is $\delta = 0$, and the two $\{\theta\}$ sets (D1) and (20) both coincide with $\{\theta\} \equiv 0$. This holds for both $\mathcal{Q}^{\mathcal{C}}_{\mathrm{glob}}$ and $\mathcal{Q}^{\mathcal{C}}_{\mathrm{loc}}$, regardless of whether the ground state is metallic or insulating. It simply reflects the fact that a change in the gauge [see Eq. (10)] has no effect whatsoever on the on-site potential, whereas it can introduce a $\mathcal{C}$-symmetry breaking in the hopping terms.

When $U = 0$ and the $\mathcal{C}$ symmetry is broken non locally by a flux φ, however, the two phase sets (D1) and (20) qualitatively differ, and one becomes more favorable with respect to the other. In particular, recalling Eqs. (10) and (11), it is straightforward to see that the phase set (D1) identifies a transformation to a gauge where the flux is described by a vector potential uniformly distributed along all the links of the ring, as pictorially sketched in Fig. 3(a), with at most a staggering δ in alternating links. Such a set Eq. (D1) turns out to be the most favorable for the global quantifier $\mathcal{Q}^{\mathcal{C}}_{\text{glob}}$, for both the metallic and insulating states. Yet, the value of the small optimal staggering $\delta = O(1/L)$ depends on the dimerization parameter r (with $\delta = 0$ for the nondimerized metallic case), implying that the $\mathcal{C}$ symmetry is least broken when the vector potential has larger magnitude in the weaker links (say w) than in the stronger links (say v). In contrast, the set (20) leads to the gauge pictorially illustrated in Fig. 3(b), where the vector potential is accumulated along the link located at P_2, i.e., on the opposite side of the ring with respect to the considered reference point P^*. This gauge turns out to be the most favorable for the local quantifier $\mathcal{Q}^{\mathcal{C}}_{\text{loc}}$, for both the metallic and the insulating states.

The different impact of the two phase sets $\{\theta_u\}$ and $\{\theta_\ell\}$ can now be illustrated by comparing the structure of the single-particle density matrix $\rho(\{\theta\})$, when evaluated in the two corresponding gauges [see Eq. (12)]. This is sketched in Fig. 8, where the ivory areas correspond to exponentially small entries of ρ, the blue areas describe how the flux phase φ is distributed in its finite-valued entries, which are highlighted as orange areas and are arranged along a diagonal stripe, whose width is determined by the correlation length λ of the quantum state. For the uniform set $\{\theta_u\}$ [see Fig. 8(a)], the flux phase φ is uniformly distributed in all entries of ρ, consistently with the corresponding gauge in Fig. 3(a). In contrast, for the phase set $\{\theta_\ell\}$ [see Fig. 8(b)], the flux phase appears only along the frame of ρ, which corresponds precisely to the point P_2 located at the opposite side of the ring with respect to the reference point P^*, as also seen in the corresponding gauge in Fig. 3(b).

The global quantifier $\mathcal{Q}^{\mathcal{C}}_{\text{glob}}$ in Eq. (40) involves all entries of ρ, through the matrix $b^{\mathcal{C}}$ in Eq. (41). In contrast, the local quantifier $\mathcal{Q}^{\mathcal{C}}_{\text{loc}}$ in Eq. (43) picks up only the (j^*, α^*)-th row of ρ, here highlighted as a dashed box, which contains the correlations between the reference point P^* (red spot) and any other site P. From Fig. 8, one can understand the different scaling laws obtained in Fig. 5(b). Indeed, when the flux is absent, i.e., for a local $\mathcal{C}$-symmetry breaking induced by the staggered on-site potential, the structure of ρ is the same in both panels of Fig. 8, and the quantifier depends only on correlation length λ, which can be identified with the localization length of the Wannier functions. While an insulator exhibits a finite localization length, the Wannier functions in a metal are delocalized and the correlations extend with a slow algebraic decay from the diagonal over the entire density matrix ρ, causing the weaker decay $\mathcal{Q}^{\mathcal{C}}_{\text{loc}} \sim 1/\sqrt{L}$ obtained in the metallic case [red curve of Fig. 5(b)], as compared to $\mathcal{Q}^{\mathcal{C}}_{\text{loc}} \sim 1/L$ found in the insulating SSH case [cyan curve of Fig. 5(b)].

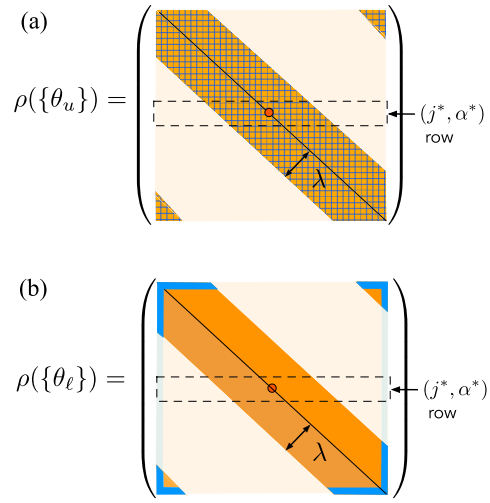

FIG. 8. Sketch of the structure of the single-particle density matrix ρ of the ground state of the SSH model with flux, evaluated in real space for two different $\{\theta\}$ phase sets. The ivory areas identify the exponentially small entries of ρ, while the cyan pattern highlights how the flux phase φ is distributed over the finite-value entries, here marked as the orange areas. (a) The case of the phase set $\{\theta_u\}$ in Eq. (D1), corresponding to the gauge illustrated in Fig. 3(a): the flux is uniformly distributed over the various ρ entries. (b) The case of the phase set $\{\theta_\ell\}$ in Eq. (20), corresponding to the gauge illustrated in Fig. 3(b), where the flux phase is accumulated in the farthest link with respect to the considered reference point P^*. The dashed box highlights the (j^*, α^*) row, which determines $\mathcal{Q}^{\mathcal{C}}_{\text{loc}}$ in Eq. (43) and describes the correlations between the chosen reference point [specifically, the site $P^* = (L/2, A)$, depicted as a red spot] and any other lattice site. An insulator is locally insensitive to a flux because in the in the local $\mathcal{C}$-breaking quantifier $\mathcal{Q}^{\mathcal{C}}_{\text{loc}}$, the flux phase only appears in the exponentially small tails located at the box ends, since the localization length λ is much smaller than the system size L.

When the $\mathcal{C}$ symmetry is broken non locally by the flux φ, however, the structure of ρ in Figs. 8(a) and 8(b) differ in the way the flux phase is distributed, and the $\{\theta_\ell\}$ is the most favorable set for $\mathcal{Q}_{\text{loc}}$. In the metallic state the correlation is quasilong ranged, i.e., the orange area extends with a power law decay over the entire row, up to the edges of the dashed box: The reference point P^* can experience the presence of the $\mathcal{C}$-breaking flux, even if accumulated at the opposite ring side. This results in the algebraic decay, $\mathcal{Q}^{\mathcal{C}}_{\text{loc}} \sim 1/\sqrt{L}$ shown in the black curve of Fig. 5(b). In contrast, because an insulator has a finite localization length λ, only sites located within such distance are correlated with P^*. The $\mathcal{C}$-breaking flux phase is present only at the ends of the dashed box in Fig. 8(b), i.e., in entries that are exponentially small in the system size, leading to the exponential suppression $\mathcal{Q}^{\mathcal{C}}_{\text{loc}} \sim \exp[-L/\Lambda]$ found in the blue curve of Fig. 5(b).

Notice that, although the flux is effectively vanishing at local level, the global quantifier Eq. (40) involves *all* entries of the single-particle density matrix ρ, including the blue corners in Fig. 8(b) where the flux phase is accumulated. For this reason, the phase set $\{\theta_\ell\}$ is the most favorable for $\mathcal{Q}^{\mathcal{C}}_{\text{loc}}$, but unfavorable for $\mathcal{Q}^{\mathcal{C}}_{\text{glob}}$ as compared to $\{\theta_u\}$.

[1] Y. Aharonov and D. Bohm, Significance of electromagnetic potentials in the quantum theory, Phys. Rev. **115**, 485 (1959).

[2] M. Peshkin and H. J. Lipkin, Topology, locality, and Aharonov-Bohm effect with neutrons, Phys. Rev. Lett. **74**, 2847 (1995).

[3] W. Kohn, Theory of the insulating state, Phys. Rev. **133**, A171 (1964).

[4] B. S. Shastry and B. Sutherland, Twisted boundary conditions and effective mass in Heisenberg-Ising and Hubbard rings, Phys. Rev. Lett. **65**, 243 (1990).

[5] N. Kawakami and S.-K. Yang, Conductivity in one-dimensional highly correlated electron systems, Phys. Rev. B **44**, 7844 (1991).

[6] H. Castella, X. Zotos, and P. Prelovsek, Integrability and ideal conductance at finite temperatures, Phys. Rev. Lett. **74**, 972 (1995).

[7] H. Watanabe and M. Oshikawa, Generalized f-sum rules and Kohn formulas on nonlinear conductivities, Phys. Rev. B **102**, 165137 (2020).

[8] H. Watanabe, Y. Liu, and M. Oshikawa, On the general properties of non-linear optical conductivities, J. Stat. Phys. **181**, 2050 (2020).

[9] J. Dalibard, F. Gerbier, G. Juzeliūnas, and P. Öhberg, Colloquium: Artificial gauge potentials for neutral atoms, Rev. Mod. Phys. **83**, 1523 (2011).

[10] N. Goldman, G. Juzeliūnas, P. Öhberg, and I. B. Spielman, Light-induced gauge fields for ultracold atoms, Rep. Prog. Phys. **77**, 126401 (2014).

[11] N. Goldman, J. C. Budich, and P. Zoller, Topological quantum matter with ultracold gases in optical lattices, Nat. Phys. **12**, 639 (2016).

[12] N. R. Cooper, J. Dalibard, and I. B. Spielman, Topological bands for ultracold atoms, Rev. Mod. Phys. **91**, 015005 (2019).

[13] P. Calabrese and J. Cardy, Time dependence of correlation functions following a quantum quench, Phys. Rev. Lett. **96**, 136801 (2006).

[14] A. Polkovnikov, K. Sengupta, A. Silva, and M. Vengalattore, Colloquium: Nonequilibrium dynamics of closed interacting quantum systems, Rev. Mod. Phys. **83**, 863 (2011).

[15] J. Eisert, M. Friesdorf, and C. Gogolin, Quantum many-body systems out of equilibrium, Nat. Phys. **11**, 124 (2015).

[16] A. Mitra, Quantum quench dynamics, Annu. Rev. Condens. Matter Phys. **9**, 245 (2018).

[17] A. De Luca, Quenching the magnetic flux in a one-dimensional fermionic ring: Loschmidt echo and edge singularity, Phys. Rev. B **90**, 081403(R) (2014).

[18] Y. O. Nakagawa, G. Misguich, M. Oshikawa, Flux quench in a system of interacting spinless fermions in one dimension, Phys. Rev. B **93**, 174310 (2016).

[19] L. Rossi and F. Dolcini, Nonlinear current and dynamical quantum phase transitions in the flux-quenched Su-Schrieffer-Heeger model, Phys. Rev. B **106**, 045410 (2022).

[20] L. D. Landau and E. M. Lifshitz, *Statistical Physics*, Part 1 (Pergamon Press, Oxford, 1959).

[21] X.-G. Wen, *Quantum Field Theory of Many-Body Systems* (Oxford University Press, Oxford, 2004).

[22] S. Ryu, A. P. Schnyder, A. Furusaki, A. W. W. Ludwig, Topological insulators and superconductors: tenfold way and dimensional hierarchy, New J. Phys. **12**, 065010 (2010).

[23] C. K. Chiu, J. C. Y. Teo, A. P. Schnyder, S. Ryu, Classification of topological quantum matter with symmetries, Rev. Mod. Phys. **88**, 035005 (2016).

[24] M. McGinley and N. R. Cooper, Topology of one-dimensional quantum systems out of equilibrium, Phys. Rev. Lett. **121**, 090401 (2018).

[25] M. McGinley and N. R. Cooper, Classification of topological insulators and superconductors out of equilibrium, Phys. Rev. B **99**, 075148 (2019).

[26] W. P. Su, J. R. Schrieffer, and A. J. Heeger, Solitons in polyacetylene, Phys. Rev. Lett. **42**, 1698 (1979).

[27] W. P. Su, J. R. Schrieffer, and A. J. Heeger, Soliton excitations in polyacetylene, Phys. Rev. B **22**, 2099 (1980).

[28] L. Rossi, J. C. Budich, and F. Dolcini, Topology in the space-time scaling limit of quantum dynamics, Phys. Rev. B **107**, L241402 (2023).

[29] In order to avoid nonlocal effects that are trivially induced by nonlocal transformations, we shall limit ourselves to the physically local transformation (1) mapping particles into holes on the same site, up to a possible phase factor.

[30] L. Rossi, F. Rossi, and F. Dolcini, Real-space effects of a quench in the Su-Schrieffer-Heeger model and elusive dynamical appearance of the topological edge states, New J. Phys. **24**, 013011 (2022).

[31] Note that the phases in Eqs. (1) and (10) differ by exhibit a factor 2, due to the nature of $\mathcal{C}$-transformation, which exchanges $c^\dagger \leftrightarrow c$.

[32] M. J. Rice and E. J. Mele, Elementary excitations of a linearly conjugated diatomic polymer, Phys. Rev. Lett. **49**, 1455 (1982).

[33] J. K. Asbóth, L. Oroszlány, and A. Pályi, *A Short Course on Topological Insulators* (Springer, Berlin, 2016).

[34] Note that the transformation (10) with the phase set Eq. (20) would break translational invariance.

[35] C. Yang, L. Li, and S. Chen, Dynamical topological invariant after a quantum quench, Phys. Rev. B **97**, 060304(R) (2018).

[36] W. Kohn, Analytic properties of Bloch waves and Wannier functions, Phys. Rev. **115**, 809 (1959).

[37] N. Marzari and D. Vanderbilt, Maximally localized generalized Wannier functions for composite energy bands, Phys. Rev. B **56**, 12847 (1997).

[38] I. Souza, N. Marzari, and D. Vanderbilt, Maximally localized Wannier functions for entangled energy bands, Phys. Rev. B **65**, 035109 (2001).

[39] N. Marzari, A. A. Mostofi, J. R. Yates, I. Souza, and D. Vanderbilt, Maximally localized Wannier functions: Theory and applications, Rev. Mod. Phys. **84**, 1419 (2012).

[40] N. Fisher, *Statistical Analysis of Circular Data* (Cambridge University Press, Cambridge, 1993).

[41] F. Ares, S. Murciano, and P. Calabrese, Entanglement asymmetry as a probe of symmetry breaking, Nat. Commun. **14**, 2036 (2023).

[42] This is certainly true if the many-particle state is Gaussian, $\boldsymbol{\rho} \propto \exp(-\sum_{I,J} c_I^\dagger M_{I,J} c_J)$ with $M^\dagger = M$, a condition that is fulfilled in all the noninteracting models considered here. In strongly interacting systems, however, signatures of the $\mathcal{C}$-breaking may appear in many-body observables only, while being absent in one-body observables.

[43] Taking into account the cell translational invariance, the presence of dimerization and the flux, we have considered phase

sets of the form $\theta_{j,A/B} = aj + \theta \pm \delta/2$, where θ, a, and δ are treated as variational parameters.

[44] Ch. Gross and W. S. Bakr, Quantum gas microscopy for single atom and spin detection, Nat. Phys. **17**, 1316 (2021).

[45] M. Cheneau, P. Barmettler, D. Poletti, M. Endres, P. Schauß, T. Fukuhara, Ch. Gross, I. Bloch, C. Kollath, and S. Kuhr, Light-cone-like spreading of correlations in a quantum many-body system, Nature (London) **481**, 484 (2012).

[46] Th. Schweigler, V. Kasper, S. Erne, I. Mazets, B. Rauer, F. Cataldini, T. Langen, Th. Gasenzer, J. Berges, and J. Schmiedmayer, Experimental characterization of a quantum many-body system via higher-order correlations, Nature (London) **545**, 323 (2017).

[47] P. W. Anderson, Absence of diffusion in certain random lattices, Phys. Rev. **109**, 1492 (1958).

[48] P. A. Lee, T. V. Ramakrishnan, Disordered electronic systems, Rev. Mod. Phys. **57**, 287 (1985).

[49] J. Fraxanet, D. González-Cuadra, T. Pfau, M. Lewenstein, T. Langen, and L. Barbiero, Topological quantum critical points in the extended bose-hubbard model, Phys. Rev. Lett. **128**, 043402 (2022).

[50] J. Voit, One-dimensional Fermi liquids, Rep. Prog. Phys. **58**, 977 (1995).

[51] L. Barbiero and L. Dell'Anna, Spreading of correlations in a quenched repulsive and attractive one-dimensional integrable system, Phys. Rev. B **96**, 064303 (2017).

[52] Y. Ge and M. Rigol, Topological phase transitions in finite-size periodically driven translationally invariant systems, Phys. Rev. A **96**, 023610 (2017).

[53] J. Motruk and F. Pollmann, Phase transitions and adiabatic preparation of a fractional Chern insulator in a boson cold-atom model, Phys. Rev. B **96**, 165107 (2017).

[54] Y.-C. He, F. Grusdt, A. Kaufman, M. Greiner, and A. Vishwanath, Realizing and adiabatically preparing bosonic integer and fractional quantum Hall states in optical lattices, Phys. Rev. B **96**, 201103(R) (2017).

[55] A. Keesling, A. Omran, H. Levine, H. Bernien, H. Pichler, S. Choi, R. Samajdar, S. Schwartz, P. Silvi, S. Sachdev, P. Zoller, M. Endres, M. Greiner, V. Vuletić, and M. D. Lukin, Quantum Kibble-Zurek mechanism and critical dynamics on a programmable Rydberg simulator, Nature (London) **568**, 207 (2019).

[56] S. Barbarino, J. Yu, P. Zoller, and J. C. Budich, Preparing atomic topological quantum matter by adiabatic nonunitary dynamics, Phys. Rev. Lett. **124**, 010401 (2020).

[57] M. Atala, M. Aidelsburger, J. T. Barreiro, D. Abanin, T. Kitagawa, E. Demler, I. Bloch, Direct measurement of the Zak phase in topological Bloch bands, Nat. Phys. **9**, 795 (2013).

[58] E. J. Meier, F. A. An, and B. Gadway, Observation of the topological soliton state in the Su-Schrieffer-Heeger model, Nat. Commun. **7**, 13986 (2016).

[59] D. Xie, W. Gou, T. Xiao, B. Gadway, and B. Yan, Topological characterizations of an extended Su–Schrieffer–Heeger model, npj Quantum Inf **5**, 55 (2019).

[60] G. H. Reid, Mingwu Lu, A. R. Fritsch, A. M. Piñeiro, and I. B. Spielman, Dynamically induced symmetry breaking and out-of-equilibrium topology in a 1D quantum system, Phys. Rev. Lett. **129**, 123202 (2022).

[61] A.-S. Walter, Z. Zhu, M. Gächter, J. Minguzzi, S. Roschinski, K. Sandholzer, K. Viebahn, and T. Esslinger, Quantization and its breakdown in a Hubbard-Thouless pump, Nat. Phys. **19**, 1471 (2023).

[62] A. Browaeys and T. Lahaye, Many-body physics with individually controlled Rydberg atoms, Nat. Phys. **16**, 132 (2020).

[63] S. de Léséleuc, V. Lienhard, P. Scholl, D. Barredo, S. Weber, N. Lang, H. P. Büchler, T. Lahaye, A. Browaeys, Observation of a symmetry-protected topological phase of interacting bosons with Rydberg atoms, Science **365**, 775 (2019).

[64] V. Lienhard, P. Scholl, S. Weber, D. Barredo, S. de Léséleuc, R. Bai, N. Lang, M. Fleischhauer, H. P. Büchler, T. Lahaye, A. Browaeys, Realization of a density-dependent Peierls phase in a synthetic, spin-orbit coupled Rydberg system, Phys. Rev. X **10**, 021031 (2020).

[65] T. Chen, C. Huang, I. Velkovsky, K. R. A. Hazzard, J. P. Covey, B. Gadway, Strongly interacting Rydberg atoms in synthetic dimensions with a magnetic flux, arXiv:2306.00883.

[66] F. Perciavalle, D. Rossini, T. Haug, O. Morsch, L. Amico, Controlled flow of excitations in a ring-shaped network of Rydberg atoms, Phys. Rev. A **108**, 023305 (2023).

[67] G. Pagano, M. Mancini, G. Cappellini, P. Lombardi, F. Schäfer, H. Hu, X.-J. Liu, J. Catani, C. Sias, M. Inguscio, and L. Fallani, A one-dimensional liquid of fermions with tunable spin, Nat. Phys. **10**, 198 (2014).

[68] X. Zhang, M. Bishof, S. L. Bromley, C. V. Kraus, M. S. Safronova, P. Zoller, A. M. Rey, J. Ye, Spectroscopic observation of SU(N)-symmetric interactions in Sr orbital magnetism, Science **345**, 1467 (2014).

[69] F. Scazza, C. Hofrichter, M. Höfer, P. C. De Groot, I. Bloch, S. Fölling, Observation of two-orbital spin-exchange interactions with ultracold SU(N)-symmetric fermions, Nat. Phys. **10**, 779 (2014).